



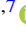




The Importance of the Upper Atmosphere to CO/O₂ Runaway on Habitable Planets Orbiting Low-mass Stars

Sukrit Ranjan^{1,2,3} , Edward W. Schwieterman^{3,4} , Michaela Leung⁴ , Chester E. Harman⁵ , and Renyu Hu^{6,7} ¹Lunar and Planetary Laboratory/Department of Planetary Sciences, University of Arizona, Tucson, AZ 85721, USA; sukrit@arizona.edu²Center for Interdisciplinary Exploration and Research in Astrophysics/Department of Physics and Astronomy, Northwestern University, Evanston, IL 60201, USA³Blue Marble Space Institute of Science, Seattle, WA 98104, USA⁴Department of Earth and Planetary Sciences, University of California at Riverside, Riverside, CA 92521, USA⁵Planetary Systems Branch, Space Science and Astrobiology Division, NASA Ames Research Center, Moffett Field, CA 94035, USA⁶Jet Propulsion Laboratory, California Institute of Technology, Pasadena, CA 91109, USA⁷Division of Geological and Planetary Sciences, California Institute of Technology, Pasadena, CA 91125, USA

Received 2023 July 17; revised 2023 October 6; accepted 2023 October 9; published 2023 November 21

Abstract

Efforts to spectrally characterize the atmospheric compositions of temperate terrestrial exoplanets orbiting M dwarf stars with JWST are now underway. Key molecular targets of such searches include O₂ and CO, which are potential indicators of life. Recently, it was proposed that CO₂ photolysis generates abundant ($\gtrsim 0.1$ bar) abiotic O₂ and CO in the atmospheres of habitable M dwarf planets with CO₂-rich atmospheres, constituting a strong false positive for O₂ as a biosignature and further complicating efforts to use CO as a diagnostic of surface biology. Importantly, this implied that TRAPPIST-1e and TRAPPIST-1f, now under observation with JWST, would abiotically accumulate abundant O₂ and CO, if habitable. Here, we use a multi-model approach to reexamine photochemical O₂ and CO accumulation on planets orbiting M dwarf stars. We show that photochemical O₂ remains a trace gas on habitable CO₂-rich M dwarf planets, with earlier predictions of abundant O₂ and CO due to an atmospheric model top that was too low to accurately resolve the unusually high CO₂ photolysis peak on such worlds. Our work strengthens the case for O₂ as a biosignature gas, and affirms the importance of CO as a diagnostic of photochemical O₂ production. However, observationally relevant false-positive potential remains, especially for O₂'s photochemical product O₃, and further work is required to confidently understand O₂ and O₃ as biosignature gases on M dwarf planets.

Unified Astronomy Thesaurus concepts: [Extrasolar rocky planets \(511\)](#); [M dwarf stars \(982\)](#); [Biosignatures \(2018\)](#); [Exoplanet atmospheric composition \(2021\)](#); [Habitable planets \(695\)](#); [Theoretical models \(2107\)](#)

1. Introduction

The launch of JWST has begun a new era in the characterization of exoplanet atmospheres. JWST has already revolutionized the study of gas giant exoplanet atmospheres, detecting novel chemical species and using them to infer operant chemical processes (Tsai et al. 2023). In the future, JWST will similarly seek to characterize the atmospheres of smaller exoplanets, including potentially habitable temperate terrestrial worlds, and such observations have already begun (Lafreniere 2017; Lewis et al. 2017; Lustig-Yaeger et al. 2019; Lim et al. 2021; Stevenson et al. 2021). Such observations may constrain surface processes such as volcanism, geochemical cycling, and the presence of life (Kaltenegger & Sasselov 2010; Kaltenegger et al. 2010; Misra et al. 2015; Krissansen-Totton et al. 2018; Faucher et al. 2020; Lehmer et al. 2020; Zhan et al. 2021; Ranjan et al. 2022).

Particularly relevant in the quest to characterize temperate terrestrial exoplanets are planets with anoxic, CO₂-rich atmospheres orbiting M dwarf stars. CO₂-rich atmospheres are expected to be ubiquitous on terrestrial exoplanets, as they are in the solar system, thanks to robust outgassing of CO₂ by basaltic magmatism (Gaillard & Scaillet 2014; Catling & Kasting 2017). Such high mean molecular mass secondary

atmospheres are only accessible to atmospheric characterization with JWST for planets orbiting M dwarf stars. Planets with CO₂-rich atmospheres orbiting M dwarf stars are therefore highly observationally relevant, and it is critical to understand their atmospheric photochemistry to accurately interpret anticipated observations of their atmospheres (Shields et al. 2016; Catling et al. 2018).

Atmospheric photochemical models of planets with CO₂-rich atmospheres orbiting M dwarf stars are historically discrepant, with observationally relevant implications for the abundance of spectroscopically active trace gases proposed as probes of surface processes. Disagreement has been particularly intense about photochemical CO and O₂ abundance in such atmospheres. While all models predicted the accumulation of photochemical CO and O₂ on CO₂-rich planets orbiting M dwarf stars, the specific predicted concentrations of CO and O₂ varied by many orders of magnitudes between models run on identical planetary scenarios (Harman et al. 2015, 2018). This is problematic because atmospheric O₂ and CO are proposed as remote probes of surface processes including the presence or absence of life (Meadows et al. 2018; Schwieterman et al. 2019; Wogan & Catling 2020). Uncertainty about the efficiency of photochemical generation of these gases neuters their value as probes of surface processes.

Recognizing the importance of this problem, extensive efforts have been invested to improve the understanding of photochemical CO and O₂ on CO₂-rich planets orbiting M dwarf stars. Initial efforts to simulate high-CO₂ atmospheres on



Original content from this work may be used under the terms of the [Creative Commons Attribution 4.0 licence](#). Any further distribution of this work must maintain attribution to the author(s) and the title of the work, journal citation and DOI.

planets orbiting M dwarf stars resulted in a disagreement of up to 4 orders of magnitude in predicted pCO and pO₂ (Domagal-Goldman et al. 2014; Tian et al. 2014; Harman et al. 2015). Harman et al. (2015) showed some of the inter-model disagreement was due to different lower boundary conditions. Harman et al. (2018) reconciled most of the remaining inter-model disagreement by showing that it was due to different assumptions regarding the photochemical effects of lightning, which generates NO_x species in a CO₂-N₂ atmosphere. These NO_x species can drive catalytic chemistry, which recombines CO and O₂ to CO₂. Upon including a lightning rate corresponding to modern Earth and its production of catalytic NO_x species, Harman et al. (2018) found photochemical O₂ to be low (pO₂ < 2 × 10⁻⁴ bar, below the false-positive threshold) across all models and planetary scenarios they considered.

Most recently, the possibility of abundant photochemical CO and O₂ was examined by Hu et al. (2020), who highlighted that previous work did not include the key NO_x reservoir species HNO₄ and N₂O₅. These species are relatively stable under M dwarf UV irradiation and serve to shuttle NO_x into the ocean due to their high solubility, reducing the efficacy of the NO_x-driven recombinative cycles. Hu et al. (2020) reproduced the results of Harman et al. (2018) for 0.05 bar CO₂ when excluding HNO₄ and N₂O₅, but found that the inclusion of HNO₄ and N₂O₅ into the photochemical network led to the generation of abundant photochemical CO and O₂, even assuming Earth-like lightning and its concomitant production of catalytic NO_x species. This mechanism is minimally affected by updated CO₂ and H₂O near-UV (NUV) cross sections (Ranjan et al. 2020) because M dwarf NUV emission is very low, rendering the photochemical effect of the updated cross sections modest for planets orbiting low-mass M dwarf stars (W. Broussard et al. 2023, in preparation). Applying this finding to the TRAPPIST-1 system, Hu et al. (2020) found that if TRAPPIST-1e and TRAPPIST-1f had enough CO₂ to be globally habitable, then they would necessarily accumulate abundant (≳0.1 bar, and possibly ≳1 bar) CO and O₂, with high O₃ as well. This atmospheric state (*CO/O₂ runaway*) would constitute an observable false positive for O₂ as a biosignature, would likely constitute a false positive for O₃ as a biosignature, and would further complicate efforts to use CO as a diagnostic of surface biology. Importantly, this false positive would persist in comparative planetological approaches to O₂ as a biosignature in the TRAPPIST-1 system, since abundant photochemical O₂ would specifically co-occur with habitable conditions on the outer planets. With observations of the TRAPPIST-1 system already underway, it is critical to confirm the prospects for the photochemical accumulation of CO and O₂ on the TRAPPIST-1 planets, to understand how to interpret potential detections of O₂, O₃, and CO.

Here, we explore further the possibility of substantial accumulation of CO and O₂ on CO₂-rich conventionally habitable planets orbiting M dwarf stars. By *conventionally habitable*, we refer to rocky planets with atmospheres and stable surface liquid water oceans, which are the prime targets for exoplanet biosignature search (Kopparapu et al. 2013; Kasting et al. 2014), as opposed to desiccated rocky planets, moist greenhouse rocky planets, Hycean worlds, or mini-Neptune aerial biospheres (Kasting 1988; Abe et al. 2011; Gao et al. 2015; Madhusudhan et al. 2021; Glidden et al. 2022). Our basic goal is to confirm whether it is possible for the photochemical decomposition of CO₂ to CO and O₂ to be

favored in conventionally habitable planet atmospheres, even with a modern Earth-like lightning rate (Harman et al. 2018; Hu et al. 2020). We place specific emphasis on O₂, which is strongly motivated by the solar system as a biosignature gas (Sagan et al. 1993), and on the TRAPPIST-1 system, now under observation by JWST. However, our findings are relevant to multiple gases and to planets orbiting M dwarf stars in general. We reproduce the CO/O₂ runaway state in two independently developed photochemical models and determine its key controls. Our multi-model approach is critical because it enables us to be confident that our findings are not due to numerical or implementation errors of individual models. We describe our methods in Section 2, report and discuss our results in Sections 3 and 4, and summarize in Section 5. We provide additional background, supporting information, and methodological details in Appendices A–E.

2. Methods

We employ two independent 1D photochemical models in our exploration of CO/O₂ runaway: the MIT Exoplanet Atmospheric Chemistry Model (MEAC; Hu et al. 2012) and Atmos (Arney et al. 2016; Lincowski et al. 2018). These models implement conceptually similar chemistry, physics, and numerical schemes, but were developed independently and share no codebase. This means that results confirmed using both models are likely to be robust to implementation errors, though they may still suffer from common-mode errors in basic physicochemical understanding (Wen et al. 1989). This intercomparative approach has proved useful in past studies employing exoplanet photochemical models, which are extremely complex, often nonlinear, and feature numerous free parameters (Harman et al. 2015, 2018; Ranjan et al. 2020). In this work, we employ MEAC and Atmos in a highly focused investigation of CO/O₂ runaway. A more exhaustive inter-comparison engaging a much broader diversity of models in a much broader range of planetary scenarios is underway in the form of the Photochemical model Intercomparison for Exoplanets (PIE) project (PI: C. E. Harman) as part of the CUISINES initiative.¹⁰

2.1. MEAC Model and Configuration.

We employ MEAC as updated by Ranjan et al. (2022), which is modified from the original Hu et al. (2012) version by elimination of errors and use of updated H₂O cross sections (Ranjan et al. 2020; Hu 2021). Importantly, this model is similar to the version of MEAC employed by Hu et al. (2020), which motivated the present work. MEAC is a 1D photochemical model that calculates the steady-state vertical trace gas composition of a planetary atmosphere given temperature–pressure and eddy diffusion (vertical transport) profiles, stellar irradiation, chemical network, and chemical boundary conditions. MEAC encodes processes including photolysis (computed via delta two-stream approximation), eddy diffusion and molecular diffusion of H and H₂, surface emission and wet and dry deposition of chemical species, diffusion-limited escape of H and H₂, and formation and deposition of S₈ and H₂SO₄ aerosols. MEAC does not account for the formation of organic haze, expected at elevated CH₄/CO₂ ratios (DeWitt et al. 2009; Arney et al. 2016); we do not explore this regime in our work.

¹⁰ <https://nexss.info/cuisines/>

We assign a high deposition velocity of $1 \times 10^{-5} \text{ cm s}^{-1}$ for C_2H_6 to account for this omission in an ad hoc fashion following Hu et al. (2012). For our full CHOSN chemical network, we consider 86 species linked by 734 reactions, corresponding to the full chemistry of Hu et al. (2012) excluding the higher hydrocarbons. Appendix E further summarizes the MEAC model setup.

2.2. Atmos Model and Configuration

Atmos is a 1D photochemical-climate model first developed by Kasting et al. (1979) and recently modified by numerous works including Arney et al. (2016), Lincowski et al. (2018), Leung et al. (2022), Teal et al. (2022). For this work, we use the publicly available version of the code¹¹ with modifications as suggested by Ranjan et al. 2020. This code has 79 species with 397 reactions including 65 photolysis reactions. Atmos also incorporates eddy diffusion, wet and dry deposition, and sulfur aerosols to simulate terrestrial environments. While not explored in this work, the model has previously been used to simulate hazy Archean-like atmospheres and has an extensive history of use for other terrestrial exoplanet applications (e.g., Domagal-Goldman et al. 2011; Arney et al. 2016, 2018; Schwieterman et al. 2019; Leung et al. 2022; Teal et al. 2022).

2.3. Planetary Scenario

We apply our photochemical models to a planetary scenario closely corresponding to the CO_2 -dominated abiotic Earth-like planet benchmark scenario detailed in Hu et al. (2012). We assume the atmospheric structure from Hu et al. (2012) ($T(z)$, $P(z)$, $K_z(z)$; Figure E2). To emphasize the enforcement of mass balance, we avoid fixed mixing ratio boundary conditions in favor of fixed surface flux and dry deposition velocity boundary conditions. We adopt surface emission of SO_2 , H_2S , CH_4 , and H_2 broadly consistent with Earth-like volcanism, surface production of CO and NO broadly consistent with Earth-like lightning, and generally low dry deposition velocities to simulate an abiotic planet (Hu et al. 2012; Harman et al. 2018; Hu & Diaz 2019) (Table 6). We set wet deposition of H_2 , O_2 , CO, CH_4 , C_2H_2 , C_2H_4 , C_2H_6 , and NH_3 to zero, to simulate saturation on a planet with abiotic oceans (Hu et al. 2012). For stellar irradiation, we adopt the TRAPPIST-1 model 1A spectrum of Peacock et al. (2019). Further details on the planet scenario are presented in Appendix E.

The high $\text{pCO}_2 = 0.9$ bar in this scenario puts it well into the CO/O_2 runaway regime identified by Hu et al. (2020). We generally avoid intermediate pCO_2 corresponding to the runaway transition itself, where sensitivity to photochemical assumptions is enhanced (Ranjan et al. 2022). This choice ensures that our modeling reflects the fundamental cause of the CO/O_2 runaway, as opposed to “red herrings”, which have enhanced importance solely in the runaway transition regime, but do not control the overall runaway phenomenon.

2.4. Photochemical Model Deployment

We perform 17 targeted simulations with a combination of MEAC and Atmos to test model and parameter sensitivities and explore CO/O_2 runaway (Table 1). This includes the stellar spectrum (including the Sun, TRAPPIST-1, and GJ 876), the partial pressure of CO_2 (pCO_2), the chemical network: the full

CHOSN network as described for both models, then chemical networks without N_2O_5 and HNO_4 (CHOSN - ($\text{N}_2\text{O}_5 + \text{HNO}_4$)), without nitrogen chemistry (CHOS), and without nitrogen and sulfur chemistry (CHO). We additionally test the impact of the shortwave UV cutoff in the stellar spectrum (λ_{crit}), the maximum altitude of the model (z_{max}) and model grid resolution (Δz), and the magnitude of vertical transport (scaled by a factor K_{scale}). The results of these tests are summarized in the last two columns of Table 1 in which we show the surface-level CO and O_2 partial pressures (pCO and pO_2 , respectively).

2.5. Synthetic Spectra

To illustrate the observational implications of our photochemical simulations, we simulate planetary transmission spectra. We simulate these synthetic spectra using the Planetary Spectrum Generator (PSG; Villanueva et al. 2018, 2022) by adapting the example presented at <https://github.com/nasaps/globes/blob/main/atmos.py>. PSG is a widely used community tool for simulating exoplanet transmission spectra (e.g., Fauchez et al. 2020; Pidhorodetska et al. 2020; Suissa et al. 2020). We choose planetary and stellar parameters consistent with our photochemical simulations (i.e., $1 M_{\oplus}$, $1 R_{\oplus}$ planet orbiting a TRAPPIST-1 like star). We include absorption due to H_2O , CH_4 , C_2H_6 , CO_2 , O_2 , O_3 , CO, H_2CO , NO, NO_2 , SO_2 , N_2O , and N_2 , as well as the effects of Rayleigh scattering, refraction, and all collision-induced absorption (CIA) included in PSG at a resolution of $R = 500$. PSG reports spectral fractional transit depths $d(\lambda)$,

$$d(\lambda) = \left(\frac{R_P + z_{\text{atm}}(\lambda)}{R_*} \right)^2, \quad (1)$$

where R_P is the solid radius of the planet, R_* is the radius of the star, and $z_{\text{atm}}(\lambda)$ is the wavelength-dependent effective height of the atmosphere. $d(\lambda)$ is specific to a given host star. To obtain a more general metric of the transmission spectrum that is not host star-specific and can be compared to other simulated transmission spectra, we also compute the effective height of the atmosphere $z_{\text{atm}}(\lambda)$ by solving Equation (1) for $z_{\text{atm}}(\lambda)$.

3. Results

3.1. Photochemistry

We find that the occurrence of CO/O_2 runaway for conventionally habitable planets with high- CO_2 atmospheres is primarily controlled by the resolution of the CO_2 photolysis peak, via the choice of z_{max} and λ_{crit} .

We find that the details of the photochemical network are not the primary control for CO/O_2 runaway. Previously, it was reported that the inclusion of N_2O_5 and HNO_4 into photochemical networks resulted in CO/O_2 runaway for CO_2 -dominated atmospheres orbiting M dwarf stars because the reactive nitrogen, which could catalyze the recombination of CO and O_2 back to CO_2 , was instead converted into HNO_4 and N_2O_5 and sequestered into the ocean. Indeed, CO/O_2 runaway is sensitive to the details of the chemical network at intermediate pCO_2 , corresponding to the onset of runaway (Table 1, Runs 8 and 9), as originally reported (Hu et al. 2020). In this intermediate atmospheric regime, sensitivity to photochemical details is enhanced because the dominant forcing on the atmosphere is changing (Ranjan et al. 2022). However, our simulations show that for CO_2 -rich atmospheres that are firmly

¹¹ <https://github.com/VirtualPlanetaryLaboratory/atmos>

Table 1
Predicted pCO and pO₂ for Our Baseline 0.9 Bar CO₂, 0.1 Bar N₂ Planetary Scenario for Different Model Assumptions

Run	Model	Star	pCO ₂ (bar)	Network	λ_{crit} (nm)	z_{max} (km)	Δz (km)	K_{scale}	pCO (bar)	pO ₂ (bar)
0	MEAC	Sun	0.9	CHOSN	110	54	1	1	5×10^{-6}	2×10^{-20}
1	MEAC	TRAPPIST-1	0.9	CHOSN	110	54	1	1	0.8	1
2	MEAC	TRAPPIST-1	0.9	CHOSN - (N ₂ O ₅ +HNO ₄)	110	54	1	1	0.8	1
3	MEAC	TRAPPIST-1	0.9	CHOS	110	54	1	1	0.8	1
4	MEAC	TRAPPIST-1	0.9	CHO	110	54	1	1	0.8	1
5	MEAC	TRAPPIST-1	0.9	CHO	110	100	1	1	0.07	1×10^{-5}
6	MEAC	TRAPPIST-1	0.9	CHO	120	54	1	1	0.07	3×10^{-4}
7	MEAC	TRAPPIST-1	0.9	CHO	120	100	1	1	0.07	1×10^{-5}
8	Atmos	TRAPPIST-1	0.9	CHOSN	117.6	100	0.5	1	0.095	1.9×10^{-4}
9	Atmos	TRAPPIST-1	0.9	CHOSN	117.6	55	0.5	1	1.65	0.13
10	MEAC	GJ 876	0.05	CHOSN	110	54	1	1	0.06	2×10^{-3}
11	MEAC	GJ 876	0.05	CHOSN - (N ₂ O ₅ +HNO ₄)	110	54	1	1	0.03	5×10^{-9}
12	MEAC	TRAPPIST-1	0.9	CHO	110	54	0.1	1	0.08	7×10^{-4}
13	MEAC	TRAPPIST-1	0.9	CHO	110	54	1	10 ³	0.26	2×10^{-4}
14	MEAC	TRAPPIST-1	0.9	CHO	110	100	1	10 ⁻³	5×10^{-8}	2×10^{-19}
15	MEAC	TRAPPIST-1	0.9	CHO	110	100	5	1	0.01	7×10^{-11}
16	MEAC	TRAPPIST-1	0.9	CHO	110	100	0.2	1	0.04	2×10^{-5}

Note. We have bolded instances of CO/O₂ runaway, which we define on an ad hoc basis as pCO > 0.1 bar and pO₂ > 0.1 bar. Assumptions regarding the details of the chemical scheme are not the main control on CO/O₂ runaway. Rather, assumptions regarding the shortwave UV cutoff and especially regarding the model top are the main control on CO/O₂ runaway, through their influence on the resolution of the CO₂ photolysis peak. This finding is multi-model.

in the runaway regime, the runaway persists when N₂O₅ and HNO₄ are removed from the photochemical network (Table 1, Runs 1 and 2). Indeed, it persists even when nitrogen and sulfur chemistry are excised entirely from the network (Table 1, Runs 3 and 4). This demonstrates that the details of the photochemical network are not the fundamental driver of CO/O₂ runaway.

Instead, CO/O₂ runaway for high-CO₂ atmospheres is driven by the choice of z_{max} and λ_{crit} . Specifically, we found that either increasing z_{max} from 54 to 100 km or increasing λ_{crit} from 110 to 120 nm was adequate to inhibit the atmosphere from becoming CO/O₂ dominated, though concentrations of both gases remained high relative to the Sun-like star case (Table 1, Runs 0, 5, and 6). Both a low λ_{crit} and a low z_{max} were required to induce a runaway. Critically, this finding is multi-model: by adjusting z_{max} from 100 to 55 km, we were able to induce CO/O₂ runaway in the independently developed Atmos photochemical model¹² as well, despite its omission of HNO₄ and N₂O₅ (Table 1, Runs 10 and 11). This confirms that λ_{crit} and z_{max} , and not the details of the photochemical network, are the main drivers of model predictions of CO/O₂ runaway.

To elucidate the mechanism by which λ_{crit} and z_{max} drive CO/O₂ runaway, we modeled atmospheres with pCO₂ = 0.01–0.1 bar (pN₂ = 0.99–0.9 bar). We explored both truncated atmospheres (model tops set at 0.34 μ bar, as in the baseline 54 km case) and extended atmospheres (model tops set at 100 km; 4 nanobar for pCO₂ = 0.1 bar). We chose this pCO₂ range because it corresponded to the onset of runaway in the truncated atmospheres, enabling us to study the numerical drivers of this phenomenon, and because at higher pCO₂, photochemical O₂/O₃ layers emerge in the truncated atmospheres, which strongly suppresses tropospheric NUV radiation and makes it hard to study the subtle changes in CO₂ and H₂O photolysis rates that ultimately drive the runaway phenomenon.

Based on our pCO₂ = 0.01–0.1 bar modeling, we attribute the influence of λ_{crit} and z_{max} on CO/O₂ runaway to their control on the model resolution of the CO₂ photolysis peak.¹³ M dwarf stars emit proportionately more of their UV radiation at far-UV (FUV) wavelengths compared to the Sun. CO₂ is a strong absorber of FUV light, and at high CO₂ abundances, this FUV radiation is absorbed high in the atmosphere (Appendix C). Terminating a high-CO₂ atmosphere at 54 km (0.34 μ bar for our baseline 0.9 bar CO₂, 0.1 bar N₂ atmosphere) results in a failure to resolve the distribution of CO₂ photolysis in the upper atmosphere with altitude (Figure 1). The failure to resolve the CO₂ FUV photolysis peak means that CO₂ photolysis, and therefore ultimately O production, is artificially confined to the topmost model grid layer. This confinement means that the O atoms that would normally be distributed across a wide altitude range are instead artificially sequestered into a single altitude bin, facilitating their mutual reaction via O+O+M \rightarrow O₂ + M (Figure 2). This is a chain termination reaction, which removes reactive power in the form of radicals from the atmosphere (Grenfell et al. 2018). In particular, the mixing ratio of OH (X_{OH}) is strongly suppressed in truncated atmospheres, and since OH is the main catalyst driving CO₂ recombination (Harman et al. 2018), it is unsurprising that as X_{OH} falls, pCO and pO₂ rise (Figure B1; Appendix B). That the CO/O₂ runaway is fundamentally driven by OH is signaled by the fact that CO increases before O₂ as pCO₂ increases. This is because OH is the only effective photochemical sink on CO (Kasting 1990), meaning variations in X_{OH} translate immediately into variations in pCO, while O₂'s sinks are more diverse and its response to X_{OH} is more indirect. In this sense, CO is the *canary in the coal mine*, signaling variations in X_{OH} in advance of O₂ (Schwieterman et al. 2016).

We conducted additional numerical experiments to confirm our explanation that CO/O₂ runaway is driven by the confinement of the O produced by CO₂ photolysis to a

¹² Arney et al. (2016); main branch, Archean template, commit b98a47527d14e6cf82e0edf4640fc7fba6d09cc8.

¹³ Specifically, the channel CO₂ + h ν \rightarrow CO + O(¹D)

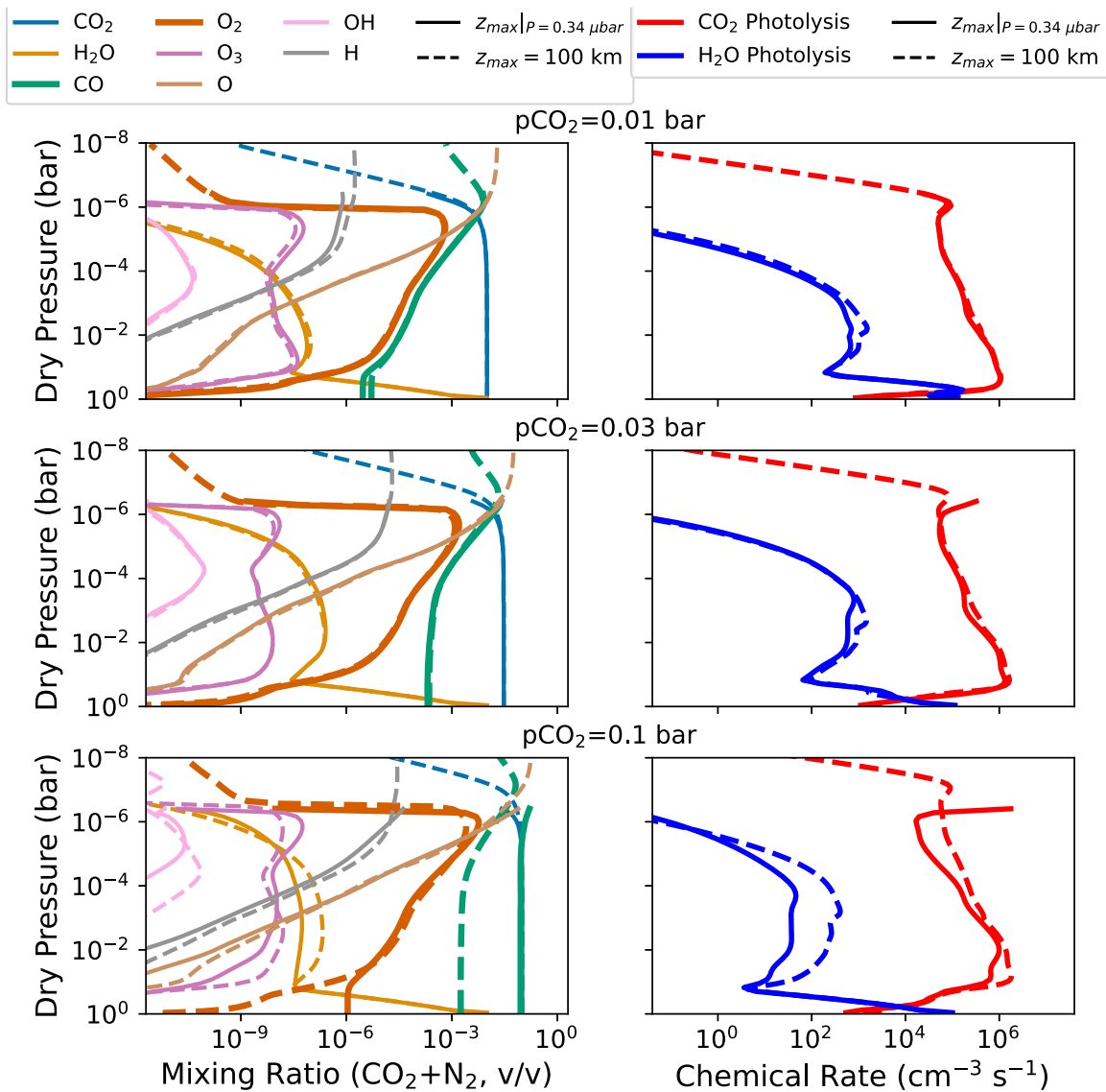


Figure 1. Non-resolution of the CO_2 photolysis peak drives CO/O_2 runaway. Concentrations of key atmospheric species (left column) and CO_2 and H_2O photolysis rates (right column) as a function of altitude, for $p\text{CO}_2 = 0.01, 0.03,$ and 0.1 bar. CHO chemistry only (S, N excluded). The key photochemical products CO and O_2 are highlighted with thicker lines in the left column. “Dry pressure” refers to the atmospheric pressure due to CO_2 and N_2 , excluding the contribution from water vapor. Solid lines correspond to calculations with the model top at $0.34 \mu\text{bar}$, while dashed lines correspond to calculations with a higher 100 km model top. At 0.01 bar, the photolysis peak is resolved by both models, and they report identical results. As $p\text{CO}_2$ increases, the CO_2 photodissociation peak moves upward and is not resolved by the calculations with the $0.34 \mu\text{bar}$ model top, resulting in large increases in $p\text{CO}$ and especially $p\text{O}_2$.

single model layer. If our explanation is correct, then more efficient vertical transport (higher $K_z(z)$) should inhibit the photochemical runaway because more of the O produced in the topmost layer of the atmosphere will be transported to lower altitudes instead of reacting with other O radicals in chain termination events. Indeed, increasing $K_z(z)$ to $K_z(z) = 10^3 K_{z,0}(z)$, where $K_{z,0}(z)$ is the eddy diffusion profile in our baseline scenario (Figure E2) suppresses $p\text{O}_2$ and $p\text{CO}$ in our baseline scenario (Table 1, Run 13). Similarly, if our explanation is correct, then increasing the number of layers in the model grid by decreasing the size of the altitude layers should inhibit runaway because the O produced by photolysis is distributed over multiple atmospheric layers instead of being limited to a single layer where it can more readily react with other O. Indeed, increasing the vertical altitude

resolution from 1 to 0.1 km suppresses $p\text{O}_2$ and $p\text{CO}$ in our baseline scenario (Table 1, Run 12).

We also investigated if we could induce a CO/O_2 runaway in an extended model grid, which resolved the CO_2 photolysis peak by varying $K_z(z)$ or the altitude resolution, and found that we could not. This suggests that models that resolve the CO_2 photodissociation peak are less sensitive to other details of the numerical scheme, as expected for physically accurate solutions. For $z_{\text{max}} = 100 \text{ km}$, we were unable to induce a CO/O_2 runaway by decreasing $K_z(z)$ by setting $K_{z,z} = 10^{-3} K_{z,0}(z)$ (Table 1, Run 14). We were similarly unable to induce a runaway by decreasing the vertical resolution by a factor of 5 to 5 km, or increasing the vertical resolution by a factor of 5 to 0.2 km. However, we noticed a weak sensitivity of $p\text{O}_2$ and $p\text{CO}$ to vertical resolution, with $p\text{O}_2$ increasing by 40% and $p\text{CO}$

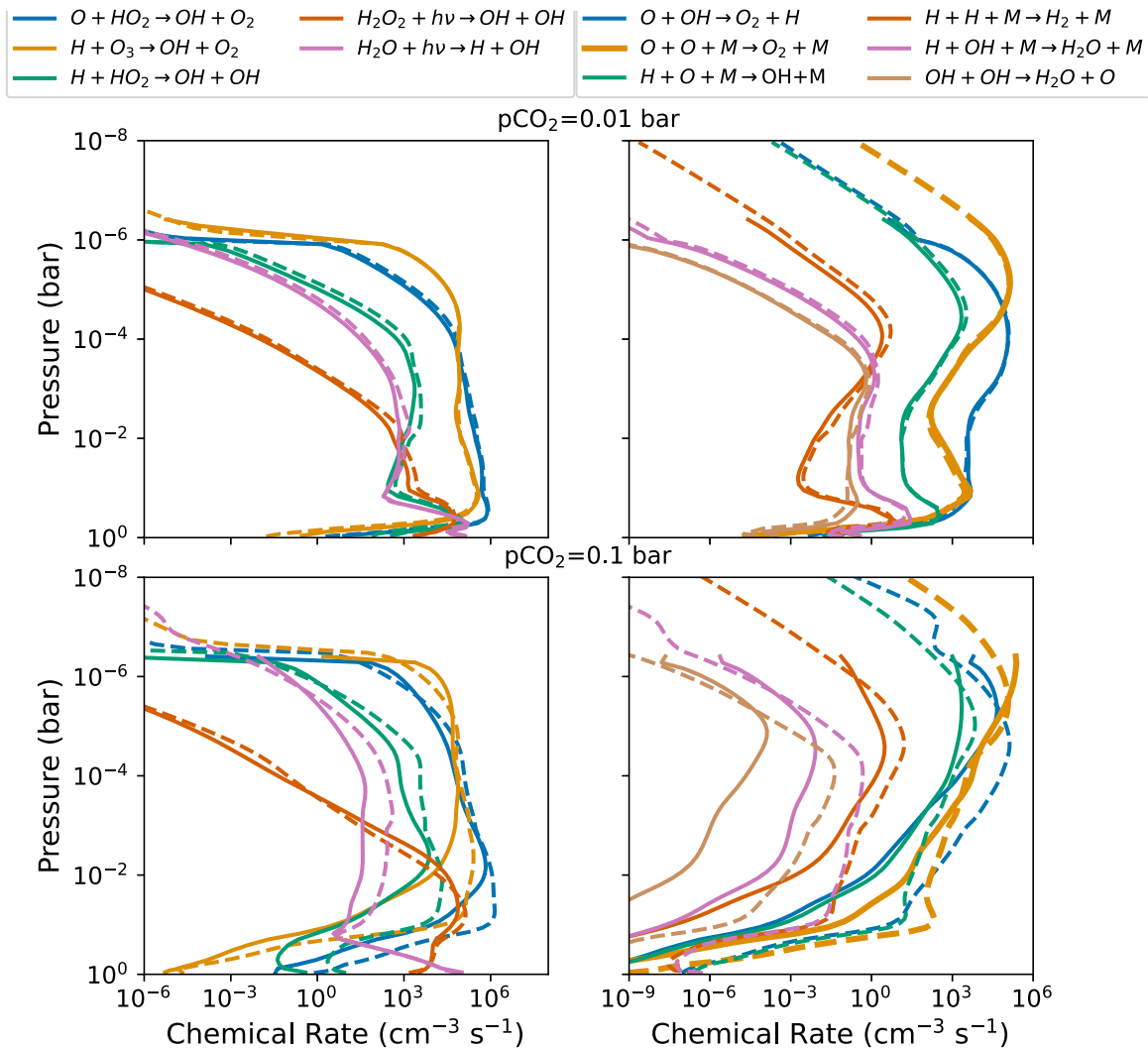


Figure 2. Vertically resolved reaction rates of key OH-producing (left column) and radical-radical (right column) reactions, for both truncated (solid lines) and extended (dashed lines) model atmospheres. The top row shows $pCO_2 = 0.01$ bar, for which both model tops return the same results, while the bottom shows $pCO_2 = 0.1$ bar, for which CO/O₂ runaway has begun in the truncated model top (but for which an NUV-attenuating ozone layer has not yet formed). CHO chemistry only (S, N excluded). The key reaction $O + O + M \rightarrow O_2 + M$ in the right column is highlighted with a thicker line. The concentration of O production in a single model bin in the truncated atmosphere leads to more intense O–O reactions, which are chain termination reactions that remove radicals from the atmosphere and impede the radical-driven recombination of CO and O₂.

decreasing by 50% as the vertical resolution increased from 1 to 0.2 km.

3.2. Synthetic Spectra

To explore the observational relevance of CO/O₂ runaway, we calculate synthetic transmission spectra of a planet in and out of CO/O₂ runaway. We specifically simulate and compare spectra of the model atmospheres corresponding to Runs 4 and 5 of Table 1, which are in and out of CO/O₂ runaway, respectively. These limited simulations do not constitute a rigorous spectral analysis of the potential observables from abiotic CO₂-rich planets orbiting M dwarf stars. Rather, they are narrowly intended to demonstrate the large amplitude of the spectral features that CO/O₂ runaway can generate, and therefore the observational relevance of better understanding this theoretical phenomenon and its triggers.

Our synthetic spectra show large variations between the runaway (Run 4) and non-runaway (Run 5) atmospheres (Figure 3). The scale of the spectral features from the runaway

atmosphere is comparable to the scale of the spectral features expected from modern Earth-like planets orbiting late M dwarf stars (Fauchez et al. 2020). The overall amplitude of the transmission spectrum is higher for the runaway case due to the lower mean molecular mass of its atmosphere. The runaway atmosphere displays stronger CO spectral features compared to the non-runaway atmosphere and O₂ and O₃ spectral features, which are absent from the non-runaway atmosphere. The runaway atmosphere displays O₃ features as strong as 50 ppm, which are absent from the non-runaway atmosphere. By comparison, JWST has already achieved a precision of <50 ppm in transmission spectroscopy, with even higher precision potentially achievable with additional observation time given the lack of evidence of a photometric noise floor down to a precision of 5 ppm (Lustig-Yaeger et al. 2023). This means that CO/O₂ runaway is observationally relevant because it can lead to spectral features that are potentially accessible to JWST. The spectral features due to CO/O₂ runaway are also relevant to other facilities such as the Large Interferometer for Exoplanets (LIFE) mission concept (Quanz et al. 2022), and

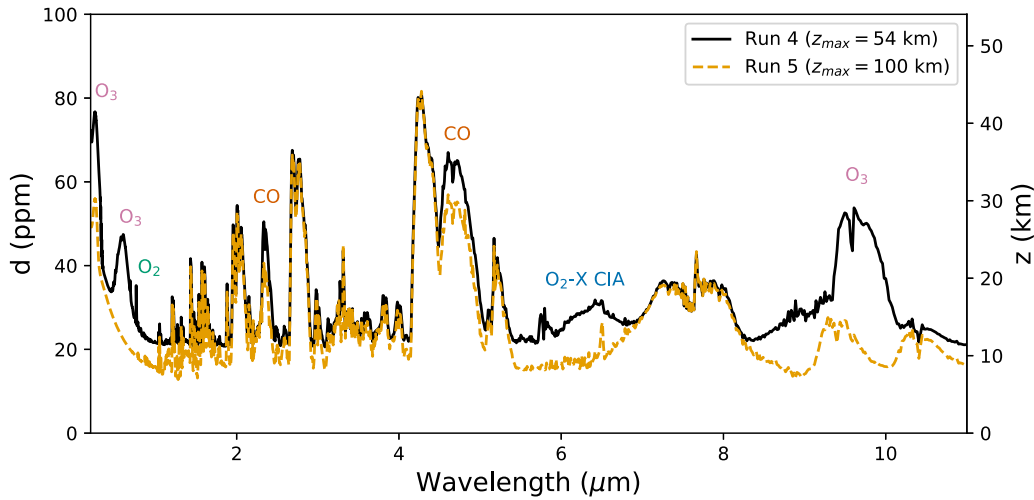


Figure 3. Simulated transmission spectra of an Earth-sized planet orbiting a late M dwarf star with a CO₂-dominated atmosphere in and out of CO/O₂ runaway, corresponding to Runs 4 and 5 of Table 1. Key molecular absorption features that differ between the runaway/non-runaway cases are highlighted. Runaway spectral features are as strong as 50 ppm and the runaway/non-runaway spectra differ by 10 s of ppm, which is potentially detectable with JWST.

potentially to ground-based facilities as well if observational challenges can be overcome (Currie et al. 2023; Hardegree-Ullman et al. 2023).

4. Discussion

Our work strengthens the case for O₂ as a biosignature gas on conventionally habitable planets orbiting M dwarf stars. Abundant atmospheric oxygen is the single strongest remotely detectable evidence of life on Earth (Sagan et al. 1993), and O₂ detection often motivates design requirements for facilities and surveys to detect life on exoplanets (Brandt & Spiegel 2014; Rodler & López-Morales 2014; Bixel & Apai 2021; Checlair et al. 2021; Hardegree-Ullman et al. 2023). However, care is required when using O₂ as a biosignature because of theoretically proposed mechanisms for the abiotic accumulation of O₂ in the atmospheres of conventionally habitable worlds (Meadows et al. 2018). In particular, it was recently argued that conventionally habitable planets with CO₂-rich atmospheres orbiting M dwarf stars would abiotically generate abundant (≥ 0.1 bar) atmospheric oxygen due to photochemical processes (Hu et al. 2020). This regime is highly observationally relevant because (1) CO₂-rich atmospheres are expected in the absence of biology, especially for planets orbiting toward the outer edge of the habitable zone (Gaillard & Scaillet 2014; Lehmer et al. 2020), and (2) due to observational biases, only planets orbiting M dwarf stars are accessible to atmospheric characterization with near-term (~ 10 – 20 yr) facilities (Shields et al. 2016). Notably, TRAPPIST-1e and f, the most observationally favorable potentially habitable exoplanets and which are already targeted by JWST observations, fall into this regime, if conventionally habitable (Wolf 2017). Our results demonstrate that the generation of abundant (≥ 0.1 bar) O₂ on conventionally habitable worlds purely through CO₂ photodissociation is unlikely, strengthening the case for O₂ as a biosignature. However, photochemical false positives remain possible for cold, desiccated worlds that are not conventionally habitable (Gao et al. 2015), and escape-driven false-positive mechanisms remain possible for a broad range of worlds (Ramirez & Kaltenegger 2014; Wordsworth & Pierrehumbert 2014; Luger & Barnes 2015; Tian 2015; Wordsworth et al. 2018).

This paper is the latest in a long series to demonstrate the extreme sensitivity of predicted photochemical concentrations of O₂ and CO in CO₂-rich conventionally habitable planet atmospheres to diverse background model assumptions, including the lightning flash rate, the absorption cross-sections of CO₂ and H₂O, the rainout rate and atmosphere/ocean redox balance, and now the altitude of the model top (Wen et al. 1989; Selsis et al. 2002; Segura et al. 2007; Harman et al. 2015, 2018; Ranjan et al. 2020). Such sensitivity is distressing given the desire to use O₂ and CO to constrain the presence or absence of biology on exoplanets (Meadows et al. 2018; Schwieterman et al. 2018, 2019; Wogan & Catling 2020), for which one desires a robust, assumption-insensitive prediction of photochemical CO or O₂.

Unfortunately, the regime of conventionally habitable planets with thick CO₂-rich atmospheres is highly sensitive to background assumptions because it corresponds to a regime with reduced atmospheric forcing from OH, permitting second-order processes to become important. The trace gas composition of modern Earth’s atmosphere is to first order controlled by OH, the “*detergent of the atmosphere*” whose reactivity is the main photochemical control on the abundances of a wide range of trace gases on modern Earth and Mars, and is thought to have done the same for much of their histories (McElroy & Donahue 1972; Parkinson & Hunten 1972; Riedel & Lassey 2008; Catling & Kasting 2017). On planets with oxic atmospheres (e.g., modern Earth), OH is robustly produced by the reaction of H₂O with O(¹D), sourced primarily from O₃ photolysis (Riedel & Lassey 2008). On anoxic planets with low CO₂ abundances (e.g., Neoproterozoic Earth) or CO₂-dominated but thin atmospheres (modern Mars), OH is robustly produced by the direct photolysis of H₂O. This robust production of OH efficiently destroys atmospheric trace gases and triggers catalytic cycles that drive the atmosphere back toward equilibrium (Harman et al. 2018). On anoxic planets with abundant CO₂ (e.g., Eoarchean Earth), this atmospheric forcing is severely inhibited because CO₂ largely competes for the same photons as H₂O, suppressing OH production (Ranjan et al. 2020). The suppression of the first-order atmospheric control from OH opens the door for second-order effects to become important, explaining the outsized relevance

of details of the photochemical scheme in this regime. This effect is amplified on planets orbiting M dwarf stars because these stars emit proportionately less light at OH-producing NUV wavelengths (Segura et al. 2005). One might be forgiven for wanting to avoid this regime entirely. However, thick CO₂-dominated atmospheres are predicted for Earth early in its history, and are predicted for conventionally habitable planets orbiting near the outer edges of their habitable zones, including the most near-term observationally accessible habitable zone planet, TRAPPIST-1e (Wolf 2017; Rugheimer & Kaltenegger 2018; Lehmer et al. 2020). Therefore, this is not a regime that can be neglected in the search for life on exoplanets.

To address this regime properly, we will need to treat the details, which are not yet fully understood in most cases. For example, the NUV cross sections of CO₂ and H₂O are still uncertain (Wen et al. 1989; Ranjan et al. 2020; W. Broussard et al. 2023, in preparation). Importantly, this means that while our results contravene the previously proposed inevitability of CO/O₂ runaway on CO₂-rich M dwarf exoplanets, they do not completely eliminate the possibility of CO/O₂ runaway because it is possible that we have omitted or incorrectly implemented one of these second-order processes. These processes are much less important (and therefore poorly constrained) in a solar system context, but may be highly relevant for M dwarf planets. In particular, our modeling neglects ion chemistry in the upper atmosphere, which may be an important source of CO and O₂ due to the thermospheric dissociation of CO₂ driven by intense M dwarf stellar energetic particle fluxes (J. Kasting, private communication, 2023 May 1). It also neglects novel photoreaction channels for H₂O, CO₂, and CO, which may be relevant in the uppermost atmosphere (An et al. 2021; Lo et al. 2021; Yang et al. 2023). We conclude that the upper atmosphere is an unexplored potential source of CO/O₂ runaway.

While our results show abundant (≥ 0.1 bar) photochemical O₂ is unlikely, they nonetheless admit the possibility of trace photochemical O₂. Our models predict abiotic pO₂ = 2×10^{-5} – 4×10^{-3} bar depending on the model branch, assumed stellar spectral energy distribution (SED), and assumed lightning flash rate. Such O₂ abundances, while comparable to biotic O₂ concentrations on Proterozoic Earth (Harman et al. 2015), do not constitute an observationally relevant biosignature false positive in the near-to-medium term because O₂ itself is undetectable at such low concentrations—even much higher, modern Earth-like O₂ concentrations (0.2 bar) will be extremely challenging to characterize with either JWST or ELTs (Faucher et al. 2020; Currie et al. 2023; Hardegree-Ullman et al. 2023). Detection of trace O₂ will likely require the advent of purpose-built instruments such as the Habitable Worlds Observatory (Checlair et al. 2021; Clery 2023), but HWO will primarily target Sun-like (FGK) stars and will therefore be relatively unaffected by M dwarf O₂ false positives (our work may be relevant to the handful of M dwarf stars on the HWO target list). More observationally relevant is the false-positive potential for O₃, which begins to produce IR spectral features in emission at 2×10^{-3} bar for M dwarf planets (Kozakis et al. 2022). This falls within the range of photochemical pO₂ produced in our modeling, meaning that photochemistry may produce observationally relevant O₃ false positives on M dwarf planets. Additionally, there remain parameters we have not explored which may expand pO₂ beyond the pO₂ = 2×10^{-5} – 4×10^{-3} range spanned by our sensitivity tests to date to model choice, lightning flash rate, and assumed stellar SED, such

as volcanic outgassing level, combustion chemistry, and temperature–pressure profile (Selsis et al. 2002; Segura et al. 2007; Hu et al. 2012; Grenfell et al. 2018; Harman et al. 2022). Lastly, oceanic chemistry may also impact pO₂. For example, the rate of direct recombination of CO and O₂ in marine waters is unconstrained, and if efficient may also suppress pO₂ and pCO (Harman et al. 2015). We highlight aqueous reactions like O₂–CO recombination as priority targets for experimental characterization relevant to understanding exoplanet atmospheres, complementing the acknowledged community priority to characterize gas-phase kinetics (Fortney et al. 2016, 2019). In summary, further theoretical and experimental work is required to establish rigorous limits on predicted trace photochemical O₂ and O₃ for CO₂-rich planets orbiting M dwarf stars, and understand their context-dependent false-positive potential.

Our work illustrates the challenges of projecting atmospheric photochemical models calibrated on solar system planets to the novel photochemical regimes accessible on exoplanets. A model top of 0.34 μ bar is capable of reproducing the trace gas composition of modern Earth (Hu et al. 2012). A model top of 0.34 μ bar is marginally adequate when modeling CO₂-rich planets orbiting Sun-like stars, for which the pressure CO₂ photodissociation peak pressure is at ≥ 1.9 μ bar (Appendix C). However, a model top of 0.34 μ bar is not adequate when modeling CO₂-rich planets orbiting M dwarf stars, for which the photodissociation peak may be as high as 0.04 μ bar (Appendix C). Care must be taken when projecting to the novel photochemical regimes accessible on exoplanets to ensure that the large diversity of background parameters in photochemical models are correctly calibrated.

Our work demonstrates the need to consider the upper atmosphere when modeling planets with CO₂-rich atmospheres orbiting M dwarf stars. Most exoplanet photochemical models, including all models currently focused on understanding O₂ false positives on temperate terrestrial worlds, focus on the lower atmosphere of the planet (troposphere, stratosphere, mesosphere) because this is the part of the atmosphere most relevant to trace gas detectability and planetary habitability. However, for CO₂-rich planets orbiting M dwarf stars, the CO₂ photodissociation peak can be well above the homopause, which corresponds to the thermosphere in the terrestrial atmosphere (Appendix D; Rumble 2017). This part of the atmosphere is partially ionized, and ion chemistry is important (Tian et al. 2008; Johnstone et al. 2018), which is rarely implemented in the exoplanet photochemistry models being used to study O₂ false positives. Similarly, above the homopause, transport is dominated by molecular diffusion, not eddy diffusion, which is not well captured for all molecules in all models (e.g., MEAC implements molecular diffusion of H and H₂ only). Accurately modeling CO₂-rich atmospheres orbiting M dwarf stars will require resolving the thermosphere, and ideally the entire atmosphere from surface to exobase. Efforts toward resolving exoplanet photochemistry in the upper atmosphere alone have been implemented for oxalic, steam, and CO₂-dominated exoplanet atmospheres (Tian 2009; Garcia-Sage et al. 2017; Johnstone et al. 2019; Johnstone 2020; Nakayama et al. 2022), and from the surface to the upper atmosphere for oxalic exoplanet atmospheres (Chen et al. 2019; Herbst et al. 2019; Cooke et al. 2023). We advocate for the extension of such work to abiotic CO₂-dominated atmospheres, which will strongly enhance our understanding of abiotic false-positive scenarios for CO and O₂.

Our findings affirm the importance of CO as a discriminant of photochemical O₂ production (Schwieterman et al. 2016; Wang et al. 2016). CO/O₂ runaway is ultimately driven by the suppression of OH, but OH is effectively the only photochemical sink on CO in conventionally habitable planet photochemical networks, while numerous pathways can suppress O₂. Consequently, when CO/O₂ runaways do occur in our model, CO rises before O₂. We can concoct scenarios where CO is scrubbed from the atmosphere while O₂ rises (e.g., through efficient surface deposition of CO but not O₂ into the ocean), but this scenario is unlikely on an abiotic planet based on our current understanding of aqueous chemistry (Kharecha et al. 2005; Harman et al. 2015; Hu et al. 2020). We therefore continue to advocate for constraining CO abundances in tandem with O₂/O₃ abundances when seeking to employ O₂ as a biosignature, as has also been argued when seeking to employ CH₄ as a biosignature (Thompson et al. 2022). Similarly, our work affirms the value of *capstone* biosignatures to corroborate potentially ambiguous primary biosignatures like O₂ (Leung et al. 2022).

5. Conclusions

We have used a multi-model approach to show that accumulation of abundant (>0.1 bar) photochemical CO and O₂ on conventionally habitable rocky planets with CO₂-rich atmospheres orbiting M dwarf stars (e.g., TRAPPIST-1e, -1f, if habitable) is unlikely, within the limits of current knowledge. An earlier prediction of abundant photochemical CO/O₂ on M dwarf planets was a model artifact, due to a model top that was too low to resolve the CO₂ photolysis peak. This model artifact occurred because on M dwarf planets with CO₂-rich atmospheres, the CO₂ photolysis peak is shifted to very high altitudes, meaning that model tops that are appropriate for solar system planets are too low for the M dwarf regime. Resolving the CO₂ photolysis peak robustly eliminates predictions of abundant (>0.1 bar) CO and O₂. However, accumulation of trace photochemical O₂ (2×10^{-4} bar < pO₂ < 0.1 bar) together with >1% CO remains a possibility. Such O₂ concentrations do not constitute an observationally relevant biosignature false positive in the near-to-medium term because they are likely too low to be detected directly with JWST, but are high enough that they may drive an observationally relevant false positive for O₃ as a biosignature, and further work is required to address this possibility. Our work demonstrates the need to accurately resolve the upper atmosphere in order to model O₂ false positives on M dwarf planets because on such worlds the CO₂ photolysis peak can extend into the heterosphere. Overall, our work strengthens the case for O₂ as a biosignature gas by reducing its false-positive potential, but further work is required to fully understand the context-dependent use of O₂ and O₃ as biosignature gases.

Acknowledgments

We thank an anonymous referee for constructive criticism that substantially improved this paper. We thank Roger Yelle and James Kasting for their helpful discussions. We thank Thomas Fauchez and Ana Glidden for their answers to questions. S.R., E.W.S., and M.L. gratefully acknowledge support by NASA Exoplanets Research Program grant No. 80NSSC22K0235. R.H. was supported by NASA Exoplanets Research Program grant No. 80NM0018F0612. This research has made use of NASA's Astrophysics Data System. The MEAC input and output files underlying Figures 1, B1, 2, and Table 1, along with the scripts

used to analyze them and to conduct the calculations presented in Appendices C and D, are publicly available at <https://github.com/sukritranjan/co-o2-runaway-revisited-toshare> and via Zenodo: doi:10.5281/zenodo.8148741 (Ranjan et al. 2023).

Software: MEAC (Hu et al. 2012), Atmos (Arney et al. 2016), PSG (Villanueva et al. 2018, 2022).

Appendix A

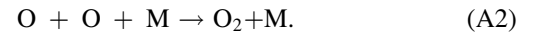
Additional Background: CO₂ Photochemical Instability on M dwarf Planets

In this appendix, we briefly review the problem of CO₂ photochemical instability, with application to M dwarf planets.

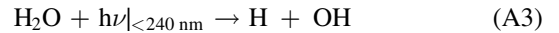
CO₂ alone is unstable to photolytic conversion to CO and O₂ in conventionally habitable planet atmospheres. CO₂ photolyzes efficiently under UV irradiation (Ityaksov et al. 2008):



The recombination reaction $\text{CO} + \text{O} + \text{M} \rightarrow \text{CO}_2 + \text{M}$ is spin forbidden and slow, leaving O₂ to accumulate via (Krasnopolsky 2019)



However, photodissociation of non-CO₂ trace gases can trigger catalytic cycles that recombine CO and O₂ back to CO₂. For example, on Mars, OH ultimately sourced from H₂O photolysis¹² (Kasting & Walker 1981; Nair et al. 1994; Harman et al. 2015; Ranjan et al. 2020):



stabilizes¹³ CO₂, via cycles like (Harman et al. 2018):



The challenge for M dwarf exoplanets is that M dwarfs emit proportionately less NUV (>200 nm) radiation due to their cooler photospheres, while their emission of FUV (<200 nm) remains robust due to their enhanced magnetic activity (Lloyd et al. 2016). At habitable temperatures, CO₂ known to photoabsorb significantly only at FUV wavelengths (Ityaksov et al. 2008), while H₂O is known to photoabsorb at both FUV and NUV wavelengths (Ranjan et al. 2020). The high FUV-to-NUV emission ratio of M dwarf stars therefore results in reduced efficacy of the H₂O photolysis-driven chemical cycles, which recombine CO₂ relative to CO₂ photolysis, resulting in predictions of enhanced CO and O₂ relative to planets orbiting M dwarf stars. The problem is exacerbated for high-CO₂ planets because abundant CO₂ shields H₂O from photodissociation, as H₂O is restricted to the lower atmosphere by condensation (Harman et al. 2015). If the relative efficacy of H₂O photolysis-driven CO₂ recombination cycles decreases below a critical point, the atmosphere can enter a state of photochemical runaway, where CO and O₂ accumulate to appreciable atmospheric concentrations; this state is termed CO/O₂ runaway (Zahnle et al. 2008; Harman et al. 2015; Hu

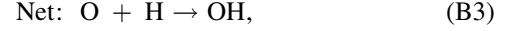
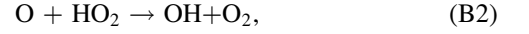
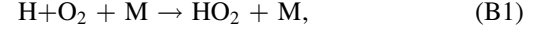
¹² While H₂O can undergo three-body photolysis as well, this only occurs at EUV wavelengths confined to the upper atmosphere, and initial sensitivity tests indicate no substantial impact on the lower atmosphere (An et al. 2021).

¹³ On Venus, CO₂ recombination is also facilitated by HCl photodissociation; this recombination mechanism is less applicable to conventionally habitable worlds with hydrological cycles, where highly soluble HCl is efficiently scrubbed from the atmosphere by rain (Demore & Yung 1982; Yung & Demore 1982; Lightowers & Cape 1988).

et al. 2020). The debate in the field has been about which conventionally habitable M dwarf planets, if any, access this CO/O₂ runaway atmospheric state (Domagal-Goldman et al. 2014; Tian et al. 2014; Gao et al. 2015; Harman et al. 2015, 2018; Hu et al. 2020). In the most recent iteration of this debate, Hu et al. (2020) find the CO/O₂ runaway regime is robustly accessed for high-CO₂ terrestrial planets orbiting M dwarf stars; in this paper, we test this finding.

stability of CO₂-rich atmospheres to photolysis. Specifically, we follow Harman et al. (2018) in constructing tables of the main catalytic cycles stabilizing CO₂ and their rates in the truncated and non-truncated atmospheres with pCO₂ = 0.1 bar (Table 2). The rate of the net catalytic cycle is set by the slowest reaction within the cycle.

The chemical cycles in the C-H-O system are complex and nonlinear, but the catalysis tables lend some insight (Harman et al. 2018). H plays a key role in recombining CO₂ because it facilitates the generation of intermediate species en route to OH:



Appendix B Catalytic Cycles in Truncated versus Non-truncated Atmospheres

In this appendix, we more closely examine the mechanism by which suppressed O abundances in truncated atmospheres lead to decreased production of OH and therefore reduced

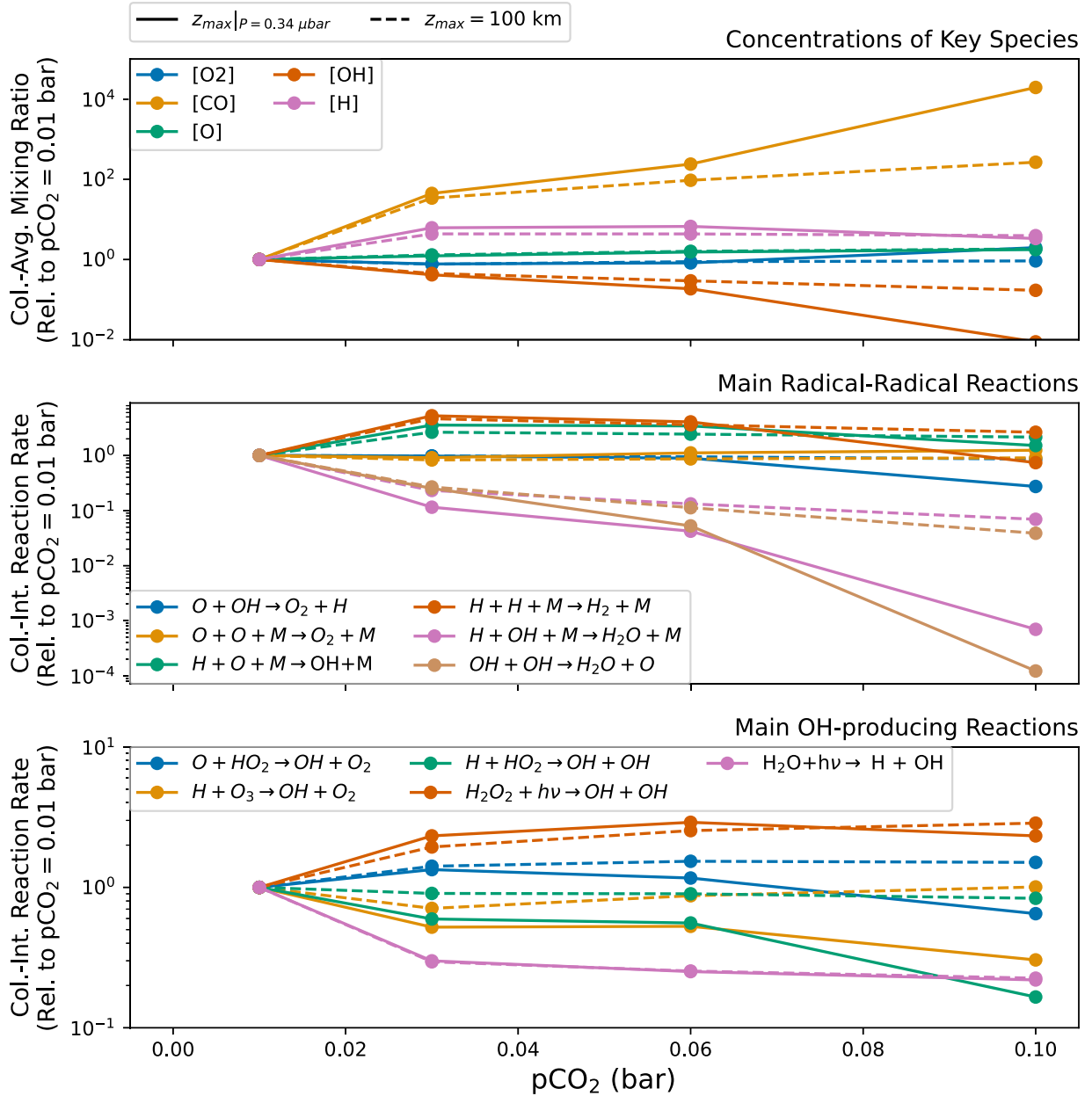


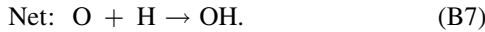
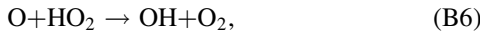
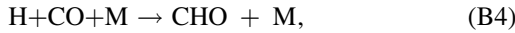
Figure B1. A closer look at the mechanics of CO/O₂ runaway. Change in column-integrated mixing ratio of key species (top) and column-integrated reaction rates for main radical-radical species (middle) and main OH-producing reactions (bottom) as a function of pCO₂, relative to pCO₂ = 0.01 for which both truncated (solid lines) and extended (dashed lines) model calculations produce the same result. Suppression in OH concentrations, likely due to suppression of OH production pathways, underlies CO/O₂ runaway.

Table 2
Column-Integrated Rates of CO₂ Photolysis and Recombination, Following Harman et al. (2018)

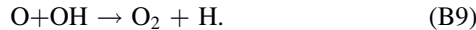
Reaction	Column-integrated Rate ($z_{\max} P=0.34 \mu\text{bar}$) ($\text{cm}^{-2} \text{s}^{-1}$)	Column-integrated Rate ($z_{\max} = 100 \text{ km}$) ($\text{cm}^{-2} \text{s}^{-1}$)
CO ₂ Photolysis		
CO ₂ + hν → CO+O	2.1E12	3.8E12
CO ₂ + hν → CO + O(¹ D)	2.6E11	1.2E11
Total CO ₂ Photolysis	2.4E12	3.9E12
CO ₂ Recombination Cycle 1		
H + O ₂ + M → HO ₂ + M	3.0E11	2.3E12
O + HO ₂ → OH + O ₂	1.0E12	2.6E12
CO+OH → CO ₂ + H	1.4E12	3.5E12
Net (CO+O → CO ₂)	3.0E11	2.3E12
CO ₂ Recombination Cycle 2		
H+CO+M → CHO+M	9.7E11	7.4E11
CHO+O ₂ → CO+HO ₂	9.6E11	7.1E11
O+HO ₂ → OH+O ₂	1.0E12	2.6E12
CO+OH → CO ₂ + H	1.4E12	3.5E12
Net (CO+O → CO ₂)	9.6E11	7.1E11
CO ₂ Recombination Cycle 3		
H ₂ O ₂ + hν → 2OH	9.5E10	1.3E11
2CO + 2OH → 2CO ₂ + 2H	7.1E11	1.8E12
2H + 2O ₂ + 2M → 2HO ₂ + 2M	1.5E11	1.1E12
2HO ₂ → H ₂ O ₂ + O ₂	8.6E10	1.0E11
Net (2CO+O ₂ → 2CO ₂)	8.6E10	1.0E11
Direct CO ₂ Recombination		
CO+O+M → CO ₂ + M	9.5E11	3.7E11
Total CO ₂ Recombination (Cycle 1 + Cycle 2 + 2×Cycle 3 + Direct Recomb.)	2.4E12	3.6E12

Note. We compare truncated and non-truncated atmospheres for pCO₂ = 0.1 bar, CHO chemistry only. Cycles 1 and 3 are ultimately drawn from the work of Stock et al. (2012) on the Martian atmosphere. Cycle 2 is identified in this work, where it is relevant to the high-CO₂, high-CO atmospheres we consider. The CO₂ recombination mechanisms we identify here balance >90% of CO₂ photolysis, meaning we have identified the main CO₂ recombination mechanisms.

and



However, OH and O are also main sources of H, via



A decrease in O therefore decreases H production, which decreases OH production, which further decreases H production, which relies on OH. This is a positive feedback loop, whereby small changes in [O] can be amplified into larger changes in [OH]. We suggest this positive feedback loop as the mechanism whereby the relatively modest changes in [O] driven by the truncated model top (Figure B1) can be amplified into relatively large changes in [OH], and therefore pCO and pO₂.

Appendix C SED-driven Changes in Photodissociation Peak Pressure

The higher FUV/NUV ratio associated with M dwarf irradiation leads to lower CO₂ photolysis peak pressures (higher CO₂ photolysis peak altitudes) relative to Sun-like stars. To illustrate this phenomenon, we derive an estimate of the pressure of peak dissociation for a well-mixed gas g in hydrostatic equilibrium, $P_{\text{peak},g}$, and apply it to CO₂ in the atmospheres of CO₂-dominated planets orbiting different stars. This calculation is crude; for example, CO₂ mixing ratios may decrease with altitude in the uppermost planetary atmosphere due to robust photolysis and diffusive separation, therefore necessitating going deeper into the atmosphere to get the same absorption compared to the well-mixed case. However, the general trends of this calculation give some intuition for why M dwarf SEDs lead to higher $P_{\text{peak},\text{CO}_2}$.

The pressure of peak photodissociation of a gas g occurs when the UV optical depth of that gas $\tau_{g,\text{UV}}$ (measured traveling from space downward normal to the planet surface) satisfies (Catling & Kasting 2017)

$$\frac{\tau_{g,\text{UV}}}{\cos(\theta_0)} = 1, \quad (\text{C1})$$

where θ_0 is the stellar angle of incidence. For an atmosphere in hydrostatic equilibrium (Catling & Kasting 2017),

$$P = \bar{\mu}gN, \quad (\text{C2})$$

where P is the pressure, μ is the mean molecular weight of the atmosphere, g is the acceleration due to gravity, and N is the number column density of the atmosphere above pressure P . Since $\tau_{\text{UV},g} = N_g \overline{\sigma_{\text{UV},g}}$, where $\overline{\sigma_{\text{UV},g}}$ is the mean UV photolysis cross section of g , for a well-mixed gas with molar concentration r_g (i.e., $N_g = r_g N$), we can substitute Equation (C2) into Equation (C1) to write

$$P_{\text{peak},g} = \frac{\cos(\theta_0) \bar{\mu}g}{r_g \overline{\sigma_{\text{UV},g}}}. \quad (\text{C3})$$

We apply Equation (C3) to estimate the peak CO₂ photolysis pressure for planets orbiting different kinds of stars for our CO₂-dominated baseline scenario. For our CO₂-dominated baseline scenario, $r_{\text{CO}_2} = 0.9$, $g = g_{\oplus}$, $\mu = 42.4$ amu, we have chosen $\theta_0 = 57.3^\circ$ (Zahnle et al. 2008). To calculate $\overline{\sigma_{\text{UV},\text{CO}_2}}$, we calculate the mean CO₂ cross-section weighted by the

Table 3
Estimates of $\overline{\sigma_{\text{UV},g}}$ and $P_{\text{peak},\text{CO}_2}$ for Different Stellar Irradiation

Star	λ_0 (nm)	$\overline{\sigma_{\text{UV},g}}$ cm^2	$P_{\text{peak},\text{CO}_2}$ (μbar)
Sun	110	2×10^{-20}	2
TRAPPIST-1	120	7×10^{-20}	0.6
TRAPPIST-1	110	9×10^{-19}	0.04

Note. The higher FUV/NUV ratio of M dwarf stars (here represented by the late M endmember TRAPPIST-1) leads to higher $\overline{\sigma_{\text{UV},g}}$ and lower $P_{\text{peak},\text{CO}_2}$ relative to Sun-like stars.

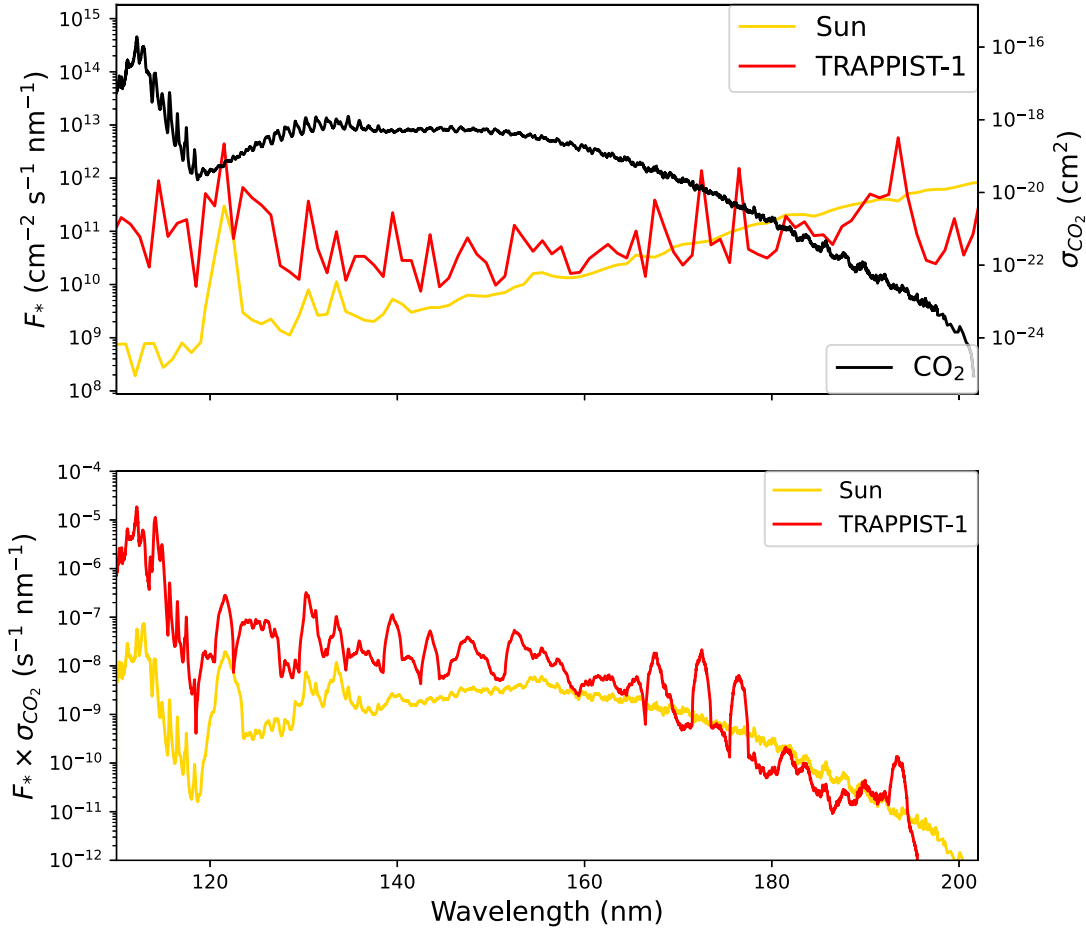


Figure C1. Top: top-of-atmosphere (TOA) number flux from the Sun and TRAPPIST-1 (left y-axis). Also co-plotted are the photolysis cross sections of CO_2 (right y-axis). Bottom: CO_2 cross sections weighted by the stellar emission of TRAPPIST-1 and the Sun. The bluer spectrum of TRAPPIST-1 increases the weight of shortwave σ_{CO_2} , which is larger, driving an increase in $\overline{\sigma_{\text{UV,g}}}$.

stellar number flux F_* :

$$\overline{\sigma_{\text{UV,g}}} = \frac{\int_{\lambda_0}^{\lambda_1} d\lambda F_*(\lambda) \sigma_{\text{CO}_2}(\lambda)}{\int_{\lambda_0}^{\lambda_1} d\lambda F_*(\lambda)}. \quad (\text{C4})$$

We calculate $\overline{\sigma_{\text{UV,CO}_2}}$ and $P_{\text{peak,CO}_2}$ for solar irradiation, TRAPPIST-1 irradiation (Peacock et al. 2019 model 1a) with $\lambda_0 = 110$ nm, and TRAPPIST-1 irradiation with $\lambda_0 = 120$ nm (Table 3). $\sigma_{\text{CO}_2}(\lambda)$ and $F_*(\lambda)$ for both scenarios are illustrated in Figure C1. In all cases, $\lambda_1 = 202$ nm, corresponding to the end of detected CO_2 absorption at room temperature (Ityaksov et al. 2008). The higher FUV/NUV ratio of TRAPPIST-1 irradiation increases $\overline{\sigma_{\text{UV,g}}}$ by $50\times$ relative to Solar irradiation, decreasing $P_{\text{peak,g}}$ proportionately. This means that to resolve the CO_2 photolysis peak correctly for planets orbiting M dwarf stars, it is necessary to extend the model grid to much lower pressures compared to planets orbiting Sun-like stars.

In this calculation, we have approximated CO_2 as well mixed. This is a good assumption for the lower atmosphere, but our extended atmospheric simulations extend into the heterosphere where CO_2 is not well mixed, and its abundance decreases with altitude. Therefore, our calculation, which assumes constant CO_2 abundance with altitude, formally constitutes a lower bound on $P_{\text{peak,CO}_2}$. Nevertheless, it illustrates the general mechanism by which $P_{\text{peak,CO}_2}$ is

decreased on planets orbiting M dwarf stars, i.e., the higher FUV/NUV ratio increasing $\overline{\sigma_{\text{UV,g}}}$.

Appendix D Homopause Estimates

In this appendix, we estimate the homopause pressure for CO_2 -dominated temperate terrestrial planets to demonstrate that the CO_2 photodissociation peak can extend into the heterosphere for M dwarf planets, demonstrating the need to resolve the upper atmosphere when modeling such worlds.

The homopause pressure is the pressure level in the atmosphere when

$$K_z(z) = D_{12}(T, n), \quad (\text{D1})$$

where $D_{12}(T, n)$ is the diffusion coefficient of gas g_1 diffusing through a background gas g_2 at temperature T and atmospheric number density n . $D_{12}(T, n)$ takes the general form (Banks & Kockart 1973)

$$D_{12}(T, n) = \frac{A_{12} T^{s_{12}}}{n}, \quad (\text{D2})$$

where A_{12} and s_{12} are specific to each (g_1, g_2) pair. Combining Equations (D1) and (D2) with the ideal gas law ($P = nkT$), we

Table 4
Homopause Estimates for Different Gases in Our CO₂-dominated Baseline Planetary Scenario

Gas	Background Gas	A_{12}	s_{12}	P_{homo} (μbar)	References
Ar	CO ₂	7.16E16	0.646	0.07	Marrero & Mason (1972)
H ₂	CO ₂	2.15E17	0.75	0.4	Marrero & Mason (1972), Hu et al. (2012)
H	CO ₂	3.87E17	0.75	0.6	Marrero & Mason (1972), Zahnle et al. (2008), Hu et al. (2012)

Note. The CO₂ photodissociation peak for CO₂-dominated atmospheres lies in the heterosphere.

can write

$$P_{\text{homo}} = \frac{kA_{12}T_{\text{homo}}^{1+s_{12}}}{K_{z,\text{homo}}}, \quad (\text{D3})$$

In Earth's upper atmosphere near the homopause, $K_z(z) = 4 \times 10^5 - 2 \times 10^6 \text{ cm}^2 \text{ s}^{-1}$, depending on which tracer is used (Hunten 1975; Swenson et al. 2019). We adopt an Earth upper atmosphere $K_{z,\text{homo},\oplus} = 1 \times 10^6 \text{ cm}^2 \text{ s}^{-1}$, which may be scaled to $K_{z,\text{homo},\text{CO}_2\text{-dominated}} = \frac{29.0}{42.4}(1 \times 10^6 \text{ cm}^2 \text{ s}^{-1}) = 7 \times 10^5 \text{ cm}^2 \text{ s}^{-1}$ for our CO₂-dominated benchmark scenario (Hu et al. 2012). Further, in the upper atmosphere, $T = 175 \text{ K}$ in our baseline scenario, meaning we can set $T_{\text{homo}} = 175 \text{ K}$. With these values, we evaluate Equation (D3) for Ar, H₂, and H diffusing through CO₂ and find homopause pressures of 0.07, 0.4, and 0.6 μbar , respectively (Table 4). For comparison, the photolysis peak pressure is 0.1 μbar for $p\text{CO}_2 = 0.1 \text{ bar}$ (Figure 1), and 0.01 μbar for $p\text{CO}_2 = 0.9 \text{ bar}$ as in our baseline scenario. This means that to accurately model the photochemistry of CO₂-rich planets orbiting M dwarf stars, it is necessary to extend model grids well into the heterosphere. We have done so here, but our calculation is not accurate because it does not accurately represent vertical transport in this part of the

atmosphere, especially molecular diffusion, and because it does not include the ion chemistry important in the thermosphere and above. We advocate for the construction of exoplanet photochemistry models that resolve the atmosphere from surface to exobase to accurately treat the important, observationally relevant problem of CO₂-rich atmospheres orbiting M dwarf stars, and especially their propensity to accumulate photochemical CO and O₂.

Appendix E Detailed Planet Scenario

In this appendix, we give more details of our planetary scenario to facilitate the reproduction of our work. Table 5 summarizes further details on our general planetary scenario and model setups. Table 6 presents the detailed species-by-species boundary conditions employed in our simulations. Figure E1 shows the stellar SEDs assumed in this work. Figure E2 shows the baseline atmospheric structure profiles ($T(z)$, $P(z)$, and $K_z(z)$) assumed in this work. In constructing the atmospheric structure profiles for the variable $p\text{CO}_2$ runs shown in Figures 1, B1, and 2, we followed Hu et al. (2012), i.e., assuming dry

Table 5
Simulation Parameters For Planetary Scenario

Scenario Parameter	MEAC	ATMOS
Model reference	Hu et al. (2012)	Arney et al. (2016)
Reaction network	As in Ranjan et al. (2022) ^a (excludes, C _{>2} -chem)	Archean Scenario (includes Ranjan et al. 2020 updates)
Stellar type	TRAPPIST-1 (Peacock et al. 2019)	TRAPPIST-1 (Peacock et al. 2019)
Stellar constant relative to modern Earth	0.592	0.592
Planet size	1 M_{\oplus} , 1 R_{\oplus}	1 M_{\oplus} , 1 R_{\oplus}
Surface albedo	0.	0.25
Major atmospheric components	0.9 bar CO ₂ , 0.1 bar N ₂ ^b	0.9 bar CO ₂ , 0.1 bar N ₂ ^b
Surface temperature ($z = 0 \text{ km}$)	288 K	288 K
Surface $r_{\text{H}_2\text{O}}$ (lowest atmospheric bin)	0.01	0.01
Eddy diffusion profile	See Figure E2	See Figure E2
Temperature–pressure profile	See Figure E2	See Figure E2
Vertical resolution	1 km	0.5 km
Rainout	Earth-like; rainout turned off for H ₂ , CO, CH ₄ , NH ₃ , N ₂ , C ₂ H ₂ , C ₂ H ₄ , C ₂ H ₆ , and O ₂ to simulate saturated ocean on an abiotic planet	Earth-like (all species)
Lightning	Simulated via $\phi_{\text{CO}}(z=0) = \phi_{\text{NO}}(z=0) = 1 \times 10^8$	On
Global redox conservation	No	No

Notes.

^a In MEAC, $p\text{N}_2$ is fixed. In Atmos, $p\text{N}_2$ is adjusted to maintain dry $P = 1 \text{ bar}$.

^b Default full chemistry CHOSN model runs contain 86 species linked by 734 reactions. For model runs where we exclude HNO₄ and N₂O₅, our network contains 84 species linked by 723 reactions. For model runs where we exclude S and N chemistry entirely, we set the initial concentrations and emission fluxes of S- and N-containing species to 0, but otherwise retain the full 734-reaction photochemical network.

Table 6
Species Choice and Treatment for the Photochemical Models Used in This Study

Species	Type MEAC	ATMOS	Surface Flux ($\text{cm}^{-2} \text{s}^{-1}$)	Surface Mixing Ratio (Relative to CO_2+N_2)	Dry Deposition Velocity (cm s^{-1})	TOA Flux ($\text{cm}^{-2} \text{s}^{-1}$)
CO_2	X	X	...	0.9	0	0
N_2	C	C	...	0.1	0	0
H_2O	X	X	...	0.01	0	0
H_2	X	X	3×10^{10}	...	0	Diffusion limited
CO	X	X	1×10^8	...	1×10^{-8}	0
CH_4	X	X	3×10^8	...	0	0
SO_2	X	X	3×10^9	...	1	0
H_2S	X	X	3×10^8	...	0.015	0
H	X	X	0	...	1	Diffusion limited
O	X	X	0	...	1	0
O(1D)	X	F	0	...	0	0
O_2	X	X	0	...	0	0
O_3	X	X	0	...	0.4	0
OH	X	X	X	...	1	0
HO_2	X	X	0	...	1	0
H_2O_2	X	X	0	...	0.5	0
CH_2O	X	X	0	...	0.1	0
CHO	X	X	0	...	0.1	0
C	X	F	0	...	0	0
CH	X	X	0	...	0	0
CH_2	X	X	0	...	0	0
$^1\text{CH}_2$	X	F	0	...	0	0
$^3\text{CH}_2$	X	X	0	...	0	0
CH_3	X	X	0	...	0	0
CH_3O	X	X	0	...	0.1	0
CH_4O	X	...	0	...	0.1	0
CHO_2	X	...	0	...	0.1	0
CH_2O_2	X	...	0	...	0.1	0
CH_3O_2	X	X	0	...	0	0
CH_4O_2	X	...	0	...	0.1	0
C_2	X	X	0	...	0	0
C_2H	X	X	0	...	0	0
C_2H_2	?	X	0	...	0	0
C_2H_3	?	X	0	...	0	0
C_2H_4	?	X	0	...	0	0
C_2H_5	X	X	0	...	0	0
C_2H_6	X	X	0	...	1×10^{-5}	0
C_2HO	X	...	0	...	0	0
$\text{C}_2\text{H}_2\text{O}$	X	...	0	...	0.1	0
$\text{C}_2\text{H}_3\text{O}$	X	...	0	...	0.1	0
$\text{C}_2\text{H}_4\text{O}$	X	...	0	...	0.1	0
$\text{C}_2\text{H}_5\text{O}$	X	...	0	...	0.1	0
S	X	X	0	...	0	0
S_2	X	X	0	...	0	0
S_3	X	F	0	...	0	0
S_4	X	F	0	...	0	0
SO	X	X	0	...	0	0
$^1\text{SO}_2$	X	F	0	...	0	0
$^3\text{SO}_2$	X	F	0	...	0	0
SO_3	X	X	0	...	1	0
HS	X	X	0	...	0	0
HSO	X	X	0	...	0	0
HSO_2	X	...	0	...	0	0
HSO_3	X	F	0	...	0.1	0
H_2SO_4	X	X	0	...	1	0
$\text{H}_2\text{SO}_4(\text{A})$	A	A	0	...	0.2	0
S_8	X	...	0	...	0	0
$\text{S}_8(\text{A})$	A	A	0	...	0.2	0
OCS	X	X	0	...	0.01	0
CS	X	X	0	...	0.01	0
CH_3S	X	...	0	...	0.01	0
CH_4S	X	...	0	...	0.01	0

Table 6
(Continued)

Species	Type MEAC	ATMOS	Surface Flux ($\text{cm}^{-2} \text{s}^{-1}$)	Surface Mixing Ratio (Relative to CO_2+N_2)	Dry Deposition Velocity (cm s^{-1})	TOA Flux ($\text{cm}^{-2} \text{s}^{-1}$)
N	X	X	0	...	0	0
NH ₃	X	...	0	...	1	0
NH ₂	X	...	0	...	0	0
NH	X	...	0	...	0	0
N ₂ O	X	...	0	...	0	0
NO	X	X	1.0×10^8	...	0.02	0
NO ₂	X	X	0	...	0.02	0
NO ₃	X	...	0	...	1	0
HNO	X	X	0	...	0	0
HNO ₂	X	F	0	...	0.5	0
HNO ₃	X	X	0	...	4	0
HCN	X	...	0	...	0.01	0
CN	X	...	0	...	0.01	0
CNO	X	...	0	...	0	0
HCNO	X	...	0	...	0	0
CH ₃ NO ₂	X	...	0	...	0.01	0
CH ₃ NO ₃	X	...	0	...	0.01	0
CH ₃ N	X	...	0	...	0	0
C ₂ H ₂ N	X	...	0	...	0	0
C ₂ H ₅ N	X	...	0	...	0	0
N ₂ H ₂	X	...	0	...	0	0
N ₂ H ₃	X	...	0	...	0	0
N ₂ H ₄	X	...	0	...	0	0
C ₃ H ₂	...	X	0	...	0	0
C ₃ H ₃	...	X	0	...	0	0
CH ₃ C ₂ H	...	X	0	...	0	0
CH ₂ CCH ₂	...	X	0	...	0	0
C ₂ H ₅ CHO	...	X	0	...	0	0
C ₂ H ₅ CHO	...	X	0	...	0	0
C ₃ H ₆	...	X	0	...	0	0
C ₃ H ₇	...	X	0	...	0	0
C ₃ H ₈	...	X	0	...	0	0
C ₂ H ₄ OH	...	X	0	...	0	0
C ₂ H ₂ OH	...	X	0	...	0	0
C ₂ H ₂ CO	...	X	0	...	0	0
C ₂ H ₃ CO	...	X	0	...	0	0
C ₂ H ₃ CHO	...	X	0	...	0	0
HCS	...	X	0	...	0	0
CS ₂	...	X	0	...	0	0
HCAER1	...	A	0	...	0	0
HCAER2	...	A	0	...	0	0

Note. (1) For species type, for each model, “X” means the full continuity-diffusion equation is solved for the species; “F” means it is treated as being in photochemical equilibrium; “A” means it is an aerosol and falls out of the atmosphere; “C” means it is treated as chemically inert; and “...” means that it is not included in that model. Note that boundary conditions like dry deposition velocity are not relevant for Type “F” species, since transport is not included for such species. The exclusion of a species from a model does not necessarily mean that the model is incapable of simulating the species, but just that it was not included in the atmospheric scenario selected here. (2) For the bottom boundary condition, either a surface flux is specified, or a surface mixing ratio. N₂ is a special case in the Kasting model and in ATMOS; in these models, [N₂] is adjusted to set the total dry pressure of the atmosphere to be 1 bar (to account for outgassed species and photochemical intermediates). Consequently, $p_{\text{N}_2} \lesssim 0.1$ bar in these models. (3) TOA flux refers to the magnitude of outflow at the TOA; hence, a negative number would correspond to an inflow. (4) For model runs where we exclude S and N chemistry entirely, the emission fluxes of S- and N-containing species to 0, but otherwise retain the full 734-reaction photochemical network.

adiabatic evolution to a 175 K stratosphere (with thermodynamic parameters drawn from Pierrehumbert 2010) and scaling modern Earth’s eddy diffusion profile by bulk atmospheric mean molecular mass.

We draw our TRAPPIST-1 spectrum from Peacock et al. (2019), model number 1A. This spectrum is binned to 1 nm resolution for use in MEAC, and to the standard Atmos model 750 point grid for use in Atmos (Lincowski et al. 2018).

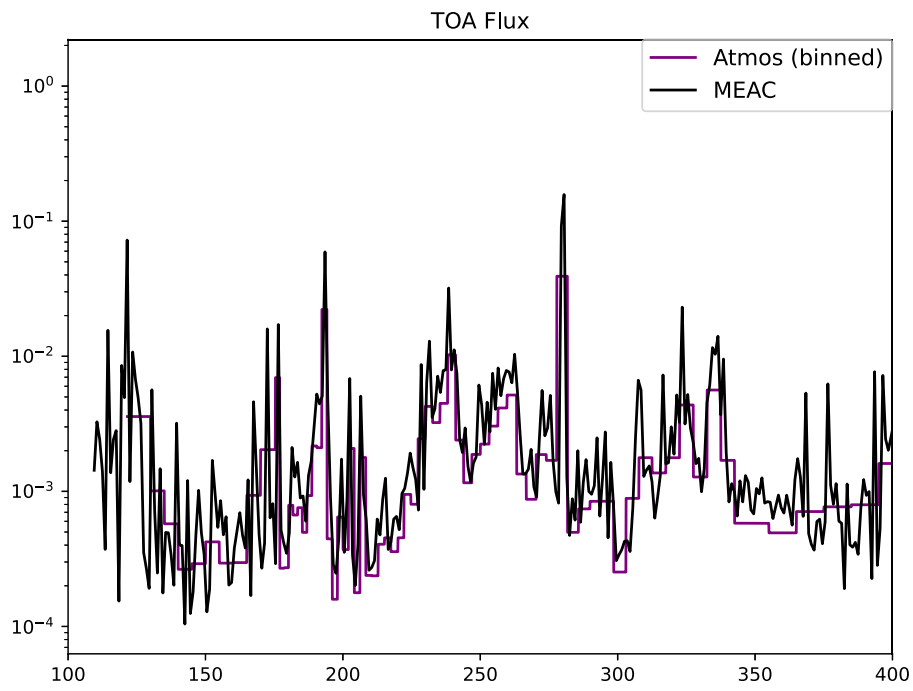


Figure E1. TRAPPIST-1 spectra employed by MEAC and Atmos in this study.

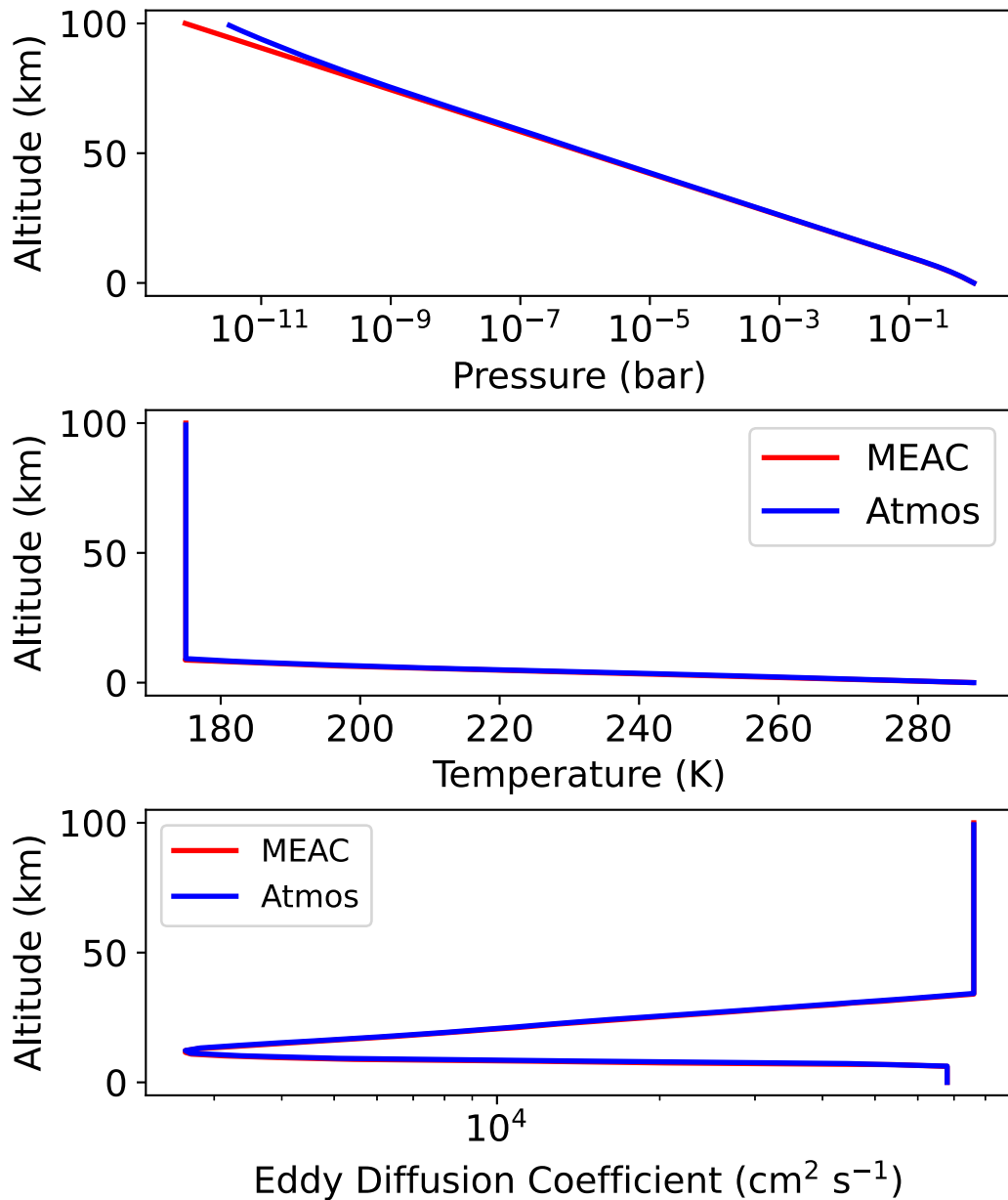






Figure E2. T - P and Eddy diffusion profiles employed by MEAC and Atmos in this study.

ORCID iDs

Sukrit Ranjan  <https://orcid.org/0000-0002-5147-9053>
 Edward W. Schwieterman  <https://orcid.org/0000-0002-2949-2163>
 Michaela Leung  <https://orcid.org/0000-0003-1906-5093>
 Chester E. Harman  <https://orcid.org/0000-0003-2281-1990>
 Renyu Hu  <https://orcid.org/0000-0003-2215-8485>

References

- Abe, Y., Abe-Ouchi, A., Sleep, N. H., & Zahnle, K. J. 2011, *AsBio*, **11**, 443
 An, S., Ranjan, S., Yuan, K., Yang, X., & Skodje, R. T. 2021, *PCCP*, **23**, 9235
 Arney, G., Domagal-Goldman, S. D., Meadows, V. S., et al. 2016, *AsBio*, **16**, 873
 Arney, G., Domagal-Goldman, S. D., & Meadows, V. S. 2018, *AsBio*, **18**, 311
 Banks, P. M., & Kockart, G. 1973, *Aeronomy (Part B)* (New York: Academic Press)
 Bixel, A., & Apai, D. 2021, *AJ*, **161**, 228
 Brandt, T. D., & Spiegel, D. S. 2014, *PNAS*, **111**, 13278
 Catling, D. C., & Kasting, J. F. 2017, *Atmospheric evolution on inhabited and lifeless worlds* (Cambridge: Cambridge Univ. Press)
 Catling, D. C., Krissansen-Totton, J., Kiang, N. Y., et al. 2018, *AsBio*, **18**, 709
 Checlair, J. H., Villanueva, G. L., Hayworth, B. P. C., et al. 2021, *AJ*, **161**, 150
 Chen, H., Wolf, E. T., Zhan, Z., & Horton, D. E. 2019, *ApJ*, **886**, 16
 Clery, D. 2023, *Sci*, **379**, 123
 Cooke, G. J., Marsh, D. R., Walsh, C., Rugheimer, S., & Villanueva, G. L. 2023, *MNRAS*, **518**, 206
 Currie, M. H., Meadows, V. S., & Rasmussen, K. C. 2023, *PSJ*, **4**, 83
 Demore, W. B., & Yung, Y. L. 1982, *Sci*, **217**, 1209
 DeWitt, H. L., Trainer, M. G., Pavlov, A. A., et al. 2009, *AsBio*, **9**, 447
 Domagal-Goldman, S. D., Meadows, V. S., Claire, M. W., & Kasting, J. F. 2011, *AsBio*, **11**, 419
 Domagal-Goldman, S. D., Segura, A., Claire, M. W., Robinson, T. D., & Meadows, V. S. 2014, *ApJ*, **792**, 90
 Fauchez, T. J., Villanueva, G. L., Schwieterman, E. W., et al. 2020, *NatAs*, **4**, 372
 Fortney, J., Robinson, T. D., Domagal-Goldman, S., et al. 2019, arXiv:1905.07064
 Fortney, J. J., Robinson, T. D., Domagal-Goldman, S., et al. 2016, arXiv:1602.06305
 Gaillard, F., & Scaillet, B. 2014, *E&PSL*, **403**, 307

- Gao, P., Hu, R., Robinson, T. D., Li, C., & Yung, Y. L. 2015, *ApJ*, **806**, 249
- Garcia-Sage, K., Gloer, A., Drake, J. J., Gronoff, G., & Cohen, O. 2017, *ApJL*, **844**, L13
- Glidden, A., Seager, S., Huang, J., Petkowski, J. J., & Ranjan, S. 2022, *ApJ*, **930**, 62
- Grenfell, J. L., Gebauer, S., Godolt, M., et al. 2018, *ApJ*, **861**, 38
- Hardegreue-Ullman, K. K., Apai, D., Bergsten, G. J., Pascucci, I., & López-Morales, M. 2023, *AJ*, **165**, 267
- Harman, C. E., Felton, R., Hu, R., et al. 2018, *ApJ*, **866**, 56
- Harman, C. E., Kopparapu, R. K., Stefánsson, G., et al. 2022, *PSJ*, **3**, 45
- Harman, C. E., Schwieterman, E. W., Schottelkotte, J. C., & Kasting, J. F. 2015, *ApJ*, **812**, 137
- Herbst, K., Grenfell, J. L., Sinnhuber, M., et al. 2019, *A&A*, **631**, A101
- Hu, R. 2021, *ApJ*, **921**, 27
- Hu, R., & Diaz, H. D. 2019, *ApJ*, **886**, 126
- Hu, R., Peterson, L., & Wolf, E. T. 2020, *ApJ*, **888**, 122
- Hu, R., Seager, S., & Bains, W. 2012, *ApJ*, **761**, 166
- Hunten, D. M. 1975, in *Astrophysics and Space Science Library, Atmospheres of Earth and the Planets*, ed. B. M. McCormac, Vol. 51 (Dordrecht: Reidel), 59
- Ityaksov, D., Linnartz, H., & Ubachs, W. 2008, *CPL*, **462**, 31
- Johnstone, C. P. 2020, *ApJ*, **890**, 79
- Johnstone, C. P., Güdel, M., Lammer, H., & Kislyakova, K. G. 2018, *A&A*, **617**, A107
- Johnstone, C. P., Khodachenko, M. L., Lüftinger, T., et al. 2019, *A&A*, **624**, L10
- Kaltenegger, L., Henning, W. G., & Sasselov, D. D. 2010, *AJ*, **140**, 1370
- Kaltenegger, L., & Sasselov, D. 2010, *ApJ*, **708**, 1162
- Kasting, J. F. 1988, *Icar*, **74**, 472
- Kasting, J. F. 1990, *OLEB*, **20**, 199
- Kasting, J. F., Kopparapu, R., Ramirez, R. M., & Harman, C. E. 2014, *PNAS*, **111**, 12641
- Kasting, J. F., Liu, S. C., & Donahue, T. M. 1979, *JGR*, **84**, 3097
- Kasting, J. F., & Walker, J. C. 1981, *JGRC*, **86**, 1147
- Kharecha, P., Kasting, J., & Siefert, J. 2005, *Gbio*, **3**, 53
- Kopparapu, R. K., Ramirez, R., Kasting, J. F., et al. 2013, *ApJ*, **765**, 131
- Kozakis, T., Mendonça, J. M., & Buchhave, L. A. 2022, *A&A*, **665**, A156
- Krasnopolsky, V. A. 2019, *Spectroscopy and Photochemistry of Planetary Atmospheres and Ionospheres. Mars, Venus, Titan, Triton and Pluto* (Cambridge: Cambridge Univ. Press)
- Krissansen-Totton, J., Garland, R., Irwin, P., & Catling, D. C. 2018, *AJ*, **156**, 114
- Lafreniere, D. 2017, NIRISS Exploration of the Atmospheric diversity of Transiting exoplanets (NEAT), JWST Proposal. Cycle 1, ID. #1201
- Lehmer, O. R., Catling, D. C., & Krissansen-Totton, J. 2020, *NatCo*, **11**, 6153
- Leung, M., Schwieterman, E. W., Parenteau, M. N., & Faucher, T. J. 2022, *ApJ*, **938**, 6
- Lewis, N., Clampin, M., Mountain, M., et al. 2017, Transit Spectroscopy of TRAPPIST-1e, JWST Proposal. Cycle 1, ID.#1331
- Lightowers, P. J., & Cape, J. N. 1988, *AtmEn*, **22**, 7
- Lim, O., Albert, L., Artigau, E., et al. 2021, Atmospheric reconnaissance of the TRAPPIST-1 planets, JWST Proposal. Cycle 1, ID. #2589
- Lincowski, A. P., Meadows, V. S., Crisp, D., et al. 2018, *ApJ*, **867**, 76
- Lo, D. Y., Yelle, R. V., Lillis, R. J., & Deighan, J. I. 2021, *Icar*, **360**, 114371
- Lloyd, R. O. P., France, K., Youngblood, A., et al. 2016, *ApJ*, **824**, 102
- Luger, R., & Barnes, R. 2015, *AsBio*, **15**, 119
- Lustig-Yaeger, J., Fu, G., May, E. M., et al. 2023, *NatAs*, *Advanced Online Publication*
- Lustig-Yaeger, J., Meadows, V. S., & Lincowski, A. P. 2019, *AJ*, **158**, 27
- Madhusudhan, N., Piette, A. A. A., & Constantinou, S. 2021, *ApJ*, **918**, 1
- Marrero, T. R., & Mason, E. A. 1972, *JPCRD*, **1**, 3
- McElroy, M. B., & Donahue, T. M. 1972, *Sci*, **177**, 986
- Meadows, V. S., Reinhard, C. T., Arney, G. N., et al. 2018, *AsBio*, **18**, 630
- Misra, A., Krissansen-Totton, J., Koehler, M. C., & Sholes, S. 2015, *AsBio*, **15**, 462
- Nair, H., Allen, M., Anbar, A. D., Yung, Y. L., & Clancy, R. T. 1994, *Icar*, **111**, 124
- Nakayama, A., Ikoma, M., & Terada, N. 2022, *ApJ*, **937**, 72
- Parkinson, T. D., & Hunten, D. M. 1972, *JATS*, **29**, 1380
- Peacock, S., Barman, T., Shkolnik, E. L., Hauschildt, P. H., & Baron, E. 2019, *ApJ*, **871**, 235
- Pidhorodetska, D., Faucher, T. J., Villanueva, G. L., Domagal-Goldman, S. D., & Kopparapu, R. K. 2020, *ApJL*, **898**, L33
- Pierrehumbert, R. T. 2010, *Principles of planetary climate* (Cambridge: Cambridge Univ. Press)
- Quanz, S. P., Ottiger, M., Fontanet, E., et al. 2022, *A&A*, **664**, A21
- Ramirez, R. M., & Kaltenegger, L. 2014, *ApJL*, **797**, L25
- Ranjan, S., Schwieterman, E. W., Harman, C., et al. 2020, *ApJ*, **896**, 148
- Ranjan, S., Seager, S., Zhan, Z., et al. 2022, *ApJ*, **930**, 131
- Ranjan, S., Schwieterman, E., Leung, M., Harman, C. E., & Hu, R., 2023 Supporting Material: "The Importance of the Upper Atmosphere to CO/O2 Runaway on Habitable Planets Orbiting Low-Mass Stars," v1.1, Zenodo, doi:10.5281/zenodo.8415538
- Riedel, K., & Lassey, K. 2008, *Water & Atmosphere*, **16**, 22, <https://www.odorox.it/wp-content/uploads/2020/05/All.pdf>
- Rodler, F., & López-Morales, M. 2014, *ApJ*, **781**, 54
- Rugheimer, S., & Kaltenegger, L. 2018, *ApJ*, **854**, 19
- Rumble, J. R. (ed.) 2017, *CRC Handbook of Chemistry and Physics* (98th edn.; Boca Raton, FL: CRC Press)
- Sagan, C., Thompson, W. R., Carlson, R., Gurnett, D., & Hord, C. 1993, *Natur*, **365**, 715
- Schwieterman, E. W., Kiang, N. Y., Parenteau, M. N., et al. 2018, *AsBio*, **18**, 663
- Schwieterman, E. W., Meadows, V. S., Domagal-Goldman, S. D., et al. 2016, *ApJL*, **819**, L13
- Schwieterman, E. W., Reinhard, C. T., Olson, S. L., et al. 2019, *ApJ*, **874**, 9
- Segura, A., Kasting, J. F., Meadows, V., et al. 2005, *AsBio*, **5**, 706
- Segura, A., Meadows, V. S., Kasting, J. F., Crisp, D., & Cohen, M. 2007, *A&A*, **472**, 665
- Selsis, F., Despois, D., & Parisot, J.-P. 2002, *A&A*, **388**, 985
- Shields, A. L., Ballard, S., & Johnson, J. A. 2016, *PhR*, **663**, 1
- Stevenson, K., Lustig-Yaeger, J., Alam, M., et al. 2021, Tell Me How I'm Supposed to Breathe With No Air: Measuring the Prevalence and Diversity of M-Dwarf Planet Atmospheres, JWST Proposal. Cycle 1
- Stock, J. W., Grenfell, J. L., Lehmann, R., Patzer, A. B. C., & Rauer, H. 2012, *P&SS*, **68**, 18
- Suissa, G., Mandell, A. M., Wolf, E. T., et al. 2020, *ApJ*, **891**, 58
- Swenson, G. R., Salinas, C. C. J. H., Vargas, F., et al. 2019, *JGRD*, **124**, 519
- Thompson, M. A., Krissansen-Totton, J., Wogan, N., Telus, M., & Fortney, J. J. 2022, *PNAS*, **119**, e2117933119
- Teal, D., Kempton, E. M.-R., Bastelberger, S., Youngblood, A., & Arney, G. 2022, *ApJ*, **927**, 90
- Tian, F. 2009, *ApJ*, **703**, 905
- Tian, F. 2015, *E&PSL*, **432**, 126
- Tian, F., France, K., Linsky, J. L., Mauas, P. J. D., & Vieytes, M. C. 2014, *E&PSL*, **385**, 22
- Tian, F., Kasting, J. F., Liu, H.-L., & Roble, R. G. 2008, *JGRE*, **113**, E05008
- Tsai, S.-M., Lee, E. K. H., Powell, D., et al. 2023, *Natur*, **617**, 483
- Villanueva, G. L., Liuzzi, G., Faggi, S., et al. 2022, *Fundamentals of the Planetary Spectrum Generator*, Vol. 617, 483, <https://psg.gsfc.nasa.gov/help.php>
- Villanueva, G. L., Smith, M. D., Protopapa, S., Faggi, S., & Mandell, A. M. 2018, *JQSTR*, **217**, 86
- Wang, Y., Tian, F., Li, T., & Hu, Y. 2016, *Icar*, **266**, 15
- Wen, J.-S., Pinto, J. P., & Yung, Y. L. 1989, *JGR*, **94**, 957
- Wogan, N. F., & Catling, D. C. 2020, *ApJ*, **892**, 127
- Wolf, E. T. 2017, *ApJL*, **839**, L1
- Wordsworth, R., & Pierrehumbert, R. 2014, *ApJL*, **785**, L20
- Wordsworth, R. D., Schaefer, L. K., & Fischer, R. A. 2018, *AJ*, **155**, 195
- Yang, J., Gudipati, M. S., Henderson, B. L., & Fleury, B. 2023, *ApJ*, **947**, 26
- Yung, Y. L., & Demore, W. B. 1982, *Icar*, **51**, 199
- Zahnle, K., Haberle, R. M., Catling, D. C., & Kasting, J. F. 2008, *JGRE*, **113**, E11004
- Zhan, Z., Seager, S., Petkowski, J. J., et al. 2021, *AsBio*, **21**, 765